Impacts of projected Arctic sea ice loss on daily weather patterns over North America

Melissa Gervais ,[a] Lantao Sun,[b] Clara Deser,[c]

[a] *Department of Meteorology and Atmospheric Science and The Institute for Computational and Data Science*

[b] *Department of Atmospheric Science, Colorado State University, Fort Collins, Colorado*

[c] *National Center for Atmospheric Research, Boulder, Colorado*

Corresponding author: Melissa Gervais, mmg62@psu.edu

ABSTRACT: Future Arctic sea ice loss has a known impact on Arctic Amplification (AA) and mean atmospheric circulation. Furthermore, several studies have shown it leads to a decreased variance in temperature over North America. In this study, we analyze results from two fully-coupled Community Earth System Model (CESM) Whole Atmosphere Community Climate Model (WACCM4) simulations with sea ice nudged to either the ensemble mean of WACCM historical runs averaged over the 1980-1999 period for the control (CTL) or projected RCP8.5 values over the 2080-2099 period for the experiment (EXP). Dominant large-scale meteorological patterns (LSMPs) are then identified using self-organizing maps applied to winter daily 500 hPa geopotential height anomalies (Z'_{500}) over North America. We investigate how sea ice loss (EXP-CTL) impacts the frequency of these LSMPs and, through composite analysis, the sensible weather associated with them. We find differences in LSMP frequency but no change in residency time indicating there is no stagnation of the flow with sea ice loss. Sea ice loss also acts to de-amplify and/or shift the Z'_{500} that characterize these LSMPs and their associated anomalies in potential temperature at 850hPa. Impacts on precipitation anomalies are more localized and consistent with changes in anomalous sea level pressure. With this LSMP framework we provide new mechanistic insights, demonstrating a role for thermodynamic, dynamic and diabatic processes in sea ice impacts on atmospheric variability. Understanding these processes from a synoptic perspective is critical as some LSMPs play an outsized role in producing the mean response to Arctic sea ice loss.

SIGNIFICANCE STATEMENT: The goal of this study is to understand how future Arctic sea ice loss might impact daily weather patterns over North America. We use a global climate model to produce on set of simulations one where sea ice is similar to present conditions and another that represents conditions at the end of the 21^{st} century. Daily patterns in large-scale circulation at roughly 5.5km in altitude are then identified using a machine learning method. We find that sea ice loss tends to de-amplify these patterns and their associated impacts on temperature nearer the surface. Our methodology allows us to probe more deeply into the mechanisms responsible for these changes, which provides a new way to understand how sea ice loss can impact the daily weather we experience.

1. Introduction

The Arctic Sea has experienced a significant decline in sea ice extent with trends of -4.36%/decade and greatest losses in the Barents/Kara Seas and Beaufort Sea (Comiso et al. 2017). Climate models project that the Arctic will become seasonally ice free by the mid 21^{st} century (Wang and Overland 2012), albeit with large uncertainty due to internal variability (Jahn et al. 2016). This sea ice loss is greatest in September; however, the impact on the atmosphere is largest in winter when turbulent heat fluxes from the ocean to the atmosphere are greatest (Deser et al. 2010; Singarayer et al. 2006).

One robust impact of sea ice loss on the atmosphere is Arctic amplification (AA), where the Arctic warms faster than the global mean (Screen and Simmonds 2010; Barnes and Screen 2015; Dai et al. 2019). The AA signal can be seen in observations (e.g. Serreze et al. 2009; Screen and Simmonds 2010) and modeling studies (e.g. Holland and Bitz 2003; Deser et al. 2010). The increased atmospheric temperatures associated with AA are largest near the surface and during the winter months (e.g. Serreze et al. 2009; Holland and Bitz 2003; Deser et al. 2010). Although the causes of AA and their relative importance remain an active area of research (Smith et al. 2019), several feedback mechanisms operating at low and high latitudes have been shown to contribute, including: the surface albedo feedback, the lapse rate feedback, and the Planck feedback (Pithan and Mauritsen 2014). Additional processes such as increased atmospheric transport of heat and moisture associated with remote SSTs have also been shown to play an important role in producing the AA signal and in particular its extension to higher altitudes (Screen et al. 2012; Perlwitz et al. 2015).

The increased turbulent heat fluxes associated with Arctic sea ice loss result in the development of localized thermal low pressure anomalies over the region of sea ice loss (Alexander et al. 2004; Gervais et al. 2016; Smith et al. 2017). The remote circulation response; however, is more uncertain (Smith et al. 2019). AA is associated with a general reduction in meridional temperature gradient and increase in mean column thickness over the Arctic which, through thermal wind arguments, is expected to weaken the midlatitude westerlies (Vihma 2014). This leads to the tug-of-war paradigm, where sea ice loss is expected to shift the midlatitude jets equatorward, while greenhouse gas forcing separate of sea ice loss acts to shift them poleward (e.g. Deser et al. 2015; Oudar et al. 2017; McCusker et al. 2017; Blackport and Kushner 2017). Fully coupled and atmosphere-only simulations with imposed future sea ice loss show broadly consistent impacts on the atmospheric circulation including a weakened Icelandic Low, an intensified Aleutian Low and Siberian High, and an equatorward shifted and often weakened zonal mean mid-latitude jet (Screen et al. 2018). However, Peings et al. (2021) showed that even with the large imposed future sea ice loss internal variability can play an important role in determining the atmospheric response.

The further impact of Arctic sea ice loss on atmospheric variability has become an important topic of discussion and disagreement. Francis and Vavrus (2012) hypothesized that AA leads to a reduction in the midlatitude westerlies and consequently more meanders in the jet. Although issues with the methodology they used were highlighted in subsequent papers (Barnes 2013; Screen et al. 2013), the topic of Arctic midlatitude linkages has been the subject of considerable research and has been summarized in numerous review articles (Cohen et al. 2014; Vihma 2014; Barnes and Screen 2015; Screen et al. 2018). More recently, Blackport and Screen (2020) extended the observational analysis to present day and found that the observed trends in waviness are no longer significant, although the AA signal has continued to increase. They conclude that the causal link is likely that periods of increased waviness leads to periods of increased AA due to enhanced meridional temperature and moisture fluxes. Much of this previous work on Arctic sea ice loss and atmospheric variability has focused on the historical period; however, in the future we expect sea ice loss to be much greater and the mechanisms through which it impacts atmospheric variability may differ from those discussed above.

Atmospheric variability can be characterized in a variety of ways that may capture different aspects and come with their own advantages or disadvantages. Many studies have utilized variance or standard deviation and found a reduction in the standard deviation of surface temperature with Arctic sea ice loss that they attribute to a reduction of the meridional temperature gradient (Screen 2014; Screen et al. 2015; Collow et al. 2019; Dai and Deng 2021). This metric is straightforward and provides useful general information about changes in temperature distribution at each location. A variety of metrics have been employed to examine changes in the waviness or sinuosity of the mid-latitude flow (e.g. Francis and Vavrus 2012, 2015; Cattiaux et al. 2016), in particular in the observations, often departures of a single geopotential height contour from its zonal mean value are used. However, early applications of such methods (Francis and Vavrus 2012) have been shown to be sensitive to analysis parameters chosen (Barnes 2013; Screen et al. 2013) thus careful attention must be paid in their application to ensure robustness across seasons and with mean warming (Cattiaux et al. 2016). These metrics provide useful information about the amplitude of spatial patterns across the Northern Hemisphere. However, neither standard deviation nor sinuosity provide information about spatial patterns, and both are limited in terms of the ability to probe more deeply into the physical mechanisms responsible.

Alternatively, the identification of large-scale meteorological patterns (LSMPs) and their changes can provide key information about regional atmospheric variability. LSMPs can be manually identified through synoptic typing; however for large datasets objective classification methods such as k-means or self-organizing maps (SOM) can be employed (Grotjahn et al. 2016). SOM is a machine learning method that can effectively identify archetypal patterns and classify data into these categories. A benefit of the SOM method is that it does not require patterns to be orthogonal, unlike the more traditional method of empirical orthogonal functions (EOFs). As a result, the SOM method can produce LSMPs (SOM nodes) that are more realistic (Grotjahn et al. 2016). Much like classic synoptic typing analysis, composite analysis of diagnostic fields can be applied to identified LSMPs. This provides a framework through which physical understanding of these patterns and their sensible weather impacts can be ascertained, which is not possible using measures of variability such as standard deviations or sinuosity.

This study will examine the impact of future Arctic sea ice loss on LSMPs of mid-tropospheric circulation over North America. We will employ two fully coupled climate model simulations with nudged sea ice to historical or projected end of 21st century conditions, thus changes are much larger than the observed trend. Self-organizing maps will be used to identify LSMPs of 500hPa geopotential height anomalies and examine their changes in frequency and pattern with sea ice loss. Composite analysis of these LSMPs will be used to investigate the sensible weather conditions associated with these LSMPs including low-level potential temperature and precipitation. Finally, the impact of sea ice loss will be viewed through the lens of these LSMPs to better understand processes tied to atmospheric variability.

2. Data and Methods

a. Model Simulations

To investigate the contribution of sea ice loss to atmospheric variability, we employed a pair of two Community Earth System Model (CESM) (Hurrell et al. 2013) simulations with constrained sea ice. The model setup utilizes the Whole Atmosphere Community Climate Model (WACCM4), the Parallel Ocean Program Version 2 (POP2), the Community Land Model Version 4 (CLM4), and the Los Alamos Sea Ice Model (CICE4) component models. The atmosphere and land components both have horizontal resolutions of $1.9°\times2.5°$, and the ocean and sea ice components have roughly $1°$ resolutions. The Whole Atmosphere Community Climate Model (WACCM4) is a high-top model with 66 vertical pressure levels reaching 5.96×10^{-6} hPa (approximately 140 km). The added vertical resolution and extension to higher heights leads to a better representation of the stratosphere. This is important for studying the impact of sea ice loss as troposphere-stratosphere interactions are known to be an important mechanism through which sea ice loss impacts the atmosphere (Sun et al. 2015). The model also includes a sophisticated stratospheric chemistry package which provides more realistic conditions in the upper-atmosphere (Marsh et al. 2013). The CICE4 model includes a thermodynamic component that calculates growth rates of snow and ice, an ice dynamics component that utilizes realistic ice physics based on ice mass and velocity, a thickness parameterization that quantifies ice strain and thickness, and a transport model that simulates ice advection (Hunke et al. 2015).

Both experiments are fully-coupled with radiative forcing held constant at the year 2000. The control simulation (CTL) sea ice is nudged to the ensemble mean of the WACCM historical runs averaged over 1980-1999 and the experiment simulation (EXP) is nudged to projected RCP 8.5

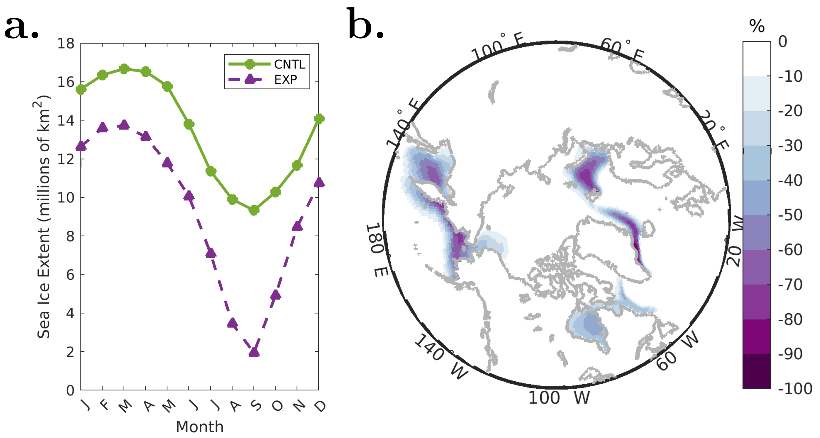

FIG. 1. a) Monthly mean sea ice extent (millions of km^2) defined as the total area of grid boxes having at least 15% sea ice concentration for the CTL (green) and EXP (purple) experiments. b) Mean difference in winter sea ice (December-February) concentration (%) between the EXP and CTL experiments.

values over 2080-2099. The nudging method is described in Deser et al. (2015) and utilizes spatially and seasonally varying long wave radiative fluxes (LRF) in each grid cell of the sea ice model to force the sea ice to mimic historical and projected sea ice conditions. The LRF is applied only to the sea ice model where there is sea ice. The magnitude of the downward LRF is larger for months of greater ice thickness and coverage, and vice versa. Although energy is not conserved using this method, water is conserved between the sea ice and ocean model components. The experiments are both 300 years in duration, but we disregard the first 100 years for spin-up time and retain only the last 200 years for the analysis.

One advantage of this coupled model configuration is that SSTs are free to vary. This allows for more realistic SSTs that are free to increase as the sea ice edge retreats and maintains dynamic atmosphere-ocean variability. Ocean-atmosphere coupling has been shown to be important for generating a more realistic response to sea ice loss that extends to lower latitudes and higher altitudes (Deser et al. 2015) and in producing a reduced summer storminess in the mid-to-late 21st century due to Arctic sea ice (Kang et al. 2023). Although the SSTs will differ between the simulations, they are still a direct bi-product of changes in sea ice as this is the only difference between the two model set-ups.

b. Self-Organizing Maps Algorithm

The SOM methodology works by repeatedly introducing input data vectors and adjusting a set of nodes to better match these input data. Each SOM node is the same size as an input data vector and is initialized prior to training, in this case with random data. These nodes are then updated throughout the training. To accomplish this, the SOM algorithm determines a best matched unit (BMU) for a specific training step (t) by finding the map node (m_c) with the smallest Euclidean distance to the input data vector ($x(t)$). The SOM is then updated using the following relation:

$$m_i(t+1) = m_i(t) + \alpha(t) \cdot h_{ci}(t) \cdot (x(t) - m_i(t)), \tag{1}$$

where $h_{ci}(t)$ is the neighborhood function that defines the relative influence on different map nodes, and $\alpha(t)$ is the learning rate parameter that defines how much the map nodes are updated (Vesanto et al. 2000; Kohonen 2001). For the neighborhood function we use the Epanechnikhov function defined as:

$$h_{ci} = max(0, 1 - \frac{d_{ci}^2}{\sigma(t)^2}), \tag{2}$$

where d is the distance between a given node (i) and the BMU (c). For the Epanechnikov function, the BMU is modified the most and this decreases with distance away from the BMU. Nodes outside of the radius of influence ($\sigma(t)$) are left unchanged. We use the diameter of the SOM as the initial radius of influence and decrease the value with each training iteration to eventually reach 1. Here we conduct two trainings with different initial $\sigma(t)$. The first training is important for broad organization and in this case has an initial $\sigma(t)$ value of 5. The second training is utilized for fine tuning and has an initial $\sigma(t)$ of 2. For the learning rate parameter we use an inverse function of training time defined as:

$$\alpha(t) = \alpha_0/(1 + 100\frac{t}{L}), \tag{3}$$

where α_0 is the initial learning rate for each training and L is the total number of training steps (t) in each training. Here we use $\alpha_0 = 0.1$ for the first training and $\alpha_0 = 0.01$ for the second training.

There are three measures used to assess SOM map quality: topological error, quantization error, and the Sammon map. Quantization error is the average Euclidean distance between the input data and their associated BMU, thus describing how similar the map nodes are to the input data vectors. The topological error is defined as the percentage of input data vectors for whom the next best match unit is not a neighbor to the BMU and thus quantifies how well-ordered the SOM is. The Sammon map is a nonlinear mapping that visually represents the relative locations of the SOM map nodes. Over-training a SOM can result in a quantization error that continues to decrease at the expense of a twisted Sammon map and higher topological error. The SOM shown here is well constructed, meaning that it has a balance of low quantization error and low topological error (<15%) and a flat Sammon map (not shown). More information about the SOM method is available in Kohonen (2001). The SOM Program Package is publicly accessible at http://www.cis.hut.fi/research/som-research/.

c. Creation of Final SOM

In this study, SOM is used to identify large-scale patterns of daily winter 500 hPa geopotential height anomalies (Z'_{500}) over North America. Analysis is conducted over the winter (December to February) season when the impact of sea ice loss on atmospheric circulation is greatest. The data is also confined the region of 25°N to 75°N and 180°E to 20°E to focus on the North American mid-latitude response to sea ice loss and identify patterns of variability on synoptic spatial scales. We are interested in identifying changes in large-scale patterns separately from the mean response to sea ice loss. As such, anomalies are computed for each simulation (CTL and EXP) separately. A daily climatology is computed for each simulation by averaging each calendar day over all 200 model years. Anomaly fields are then created by subtracting the daily climatology, for the corresponding simulation and calendar day, from each day of the simulation. This procedure takes into account the seasonal cycle of Z_{500} so that anomalies are identified across all months and effectively removes the seasonally varying mean response to sea ice loss. For subsequent analysis, the term "anomalies" will refer to the difference in any field relative to its seasonally varying climatology and these will be denoted with a prime, for example Z'_{500}.

There are several options for pre-processing input data depending on the research question. In this study, the Z'_{500} fields are normalized by removing the mean of the time series and dividing by the standard deviation at each grid point prior to training. This ensures that locations that experience greater variability do not have a larger impact on the SOM classification. The data are then multiplied by the cosine of the latitude to account for grid box area changes with latitude. Input data for the SOM consists of model output from both the CTL and EXP simulations to ensure all patterns of variability present in each simulation are represented in the final SOM.

The SOM algorithm includes several user defined parameters, the most notable being the number of map nodes (archetypal patterns). Here the number of map nodes is determined through testing a variety of different SOM sizes. A final SOM size is chosen that is the smallest size that is able to identify all patterns that are physically relevant to the research question. After testing different SOM sizes, a 5×3 grid of map nodes for a total of 15 nodes was chosen for this study. For well constructed SOMs, such as that presented here, Gervais et al. (2016) found that changes in user defined parameters (e.g. neighborhood function and learning rate parameter) made little difference in the final SOM.

d. SOM Analysis

Once a SOM is trained, the final nodes or LSMPs are no longer modified and each day input data vector (or day of data in this case) is compared to the final SOM and assigned a BMU. This enables a multitude of additional analyses to explore the LSMPs. The frequency of occurrence of each LSMP is computed as the total number of BMUs for a given node divided by the total number of input days for the entire SOM. This can provide information about which LSMPs are most common. We can also obtain a more complete understanding of the physical processes associated with each node through compositing of any variable of interest. These composites (S) are computed for a given node by averaging all days that are assigned as a BMU for that node. For both the frequency (f) and composite, calculations can include all of the input data or only the BMUs associated with either the CTL (f_{CTL} or S_{CTL}) or EXP (f_{EXP} or S_{EXP}).

Differences in atmospheric variability between experiments can arise from either differences in the frequency of SOM nodes ($\Delta f = f_{EXP} - f_{CTL}$) or differences in their pattern ($\Delta S = S_{EXP} - S_{CTL}$). The relative importance of changes in frequency versus change in pattern will depend on the SOM size. With a smaller SOM we would expect changes in pattern to be greater and for a larger SOM we would expect to see more changes in frequency. Examining both metrics together provides a complete view of changes in the variability (Gervais et al. 2020). Throughout the paper, these differences will be described as the impact of sea ice loss on the either the frequency or pattern.

Significant differences in frequency are evaluated using a permutation test. Here BMUs from both simulations are randomly assigned to new "CTL" and "EXP" labels and a new Δf is computed. This process is repeated 1000 times in order to create a null distribution of Δf values. If the true Δf lies outside the 2.5^{th} or 97.5^{th} percentiles, the frequency differences are deemed significant. This process is repeated for each node. Statistical significance for ΔS at each grid point is determined using a student's t-test at a 95% confidence level with a null hypothesis of zero.

The SOM categorizes each day into different LSMPs with a given f and S. Thus, the seasonal mean field of a given experiment can be approximated as the sum of the frequencies of each node times their composite. As discussed in Gervais et al. (2020), the total difference between simulations ($\Delta(fS)$) for all nodes can then be approximately decomposed into contributions from changes in frequency and pattern as follows:

$$\Delta(fS) = \Delta f S_{avg} + f_{avg} \Delta S \tag{4}$$

where,

$$\Delta(fS) = \sum_{i=1}^{n} f_{ei} S_{ei} - \sum_{i=1}^{n} f_{ci} S_{ci} \tag{5}$$

$$\Delta f S_{avg} = \sum_{i=1}^{n} (f_{ei} - f_{ci}) \frac{S_{ei} + S_{ci}}{2} \tag{6}$$

$$f_{avg} \Delta S = \sum_{i=1}^{n} \frac{f_{ei} + f_{ci}}{2} (S_{ei} - S_{ci}) \tag{7}$$

In these equations, n is the number of SOM nodes (which in the case of our SOM is 15), and the indices c and e indicate the CTL and EXP simulations respectively. This decomposition can be conducted for any variable of choice to understand the impact of frequency versus pattern associated with these LSMPs.

3. Results and Discussion

a. Winter Atmospheric Response to Sea Ice Loss

The atmospheric response to future sea ice loss will be defined in this study as the difference between the CTL and EXP simulations (EXP - CTL). The differences in sea ice cover between the simulations are seasonally varying with the greatest differences in September coinciding with the seasonal sea ice minimum (Fig. 1a). Although sea ice loss is greatest in September, the mean impact on atmospheric circulation is greatest in the winter, consistent with previous studies (Vihma 2014). This seasonality of the atmospheric response can be seen in the monthly mean differences in 500 hPa geopotential height (Z_{500}) and sea level pressure (SLP) between the simulations (Fig. S1). The winter mean atmospheric response to future sea ice loss shows a clear signal of Arctic Amplification with warmer potential temperatures at 850 hPa (Θ_{850}) that are greatest at the high latitudes (Fig. 2a). Consistent with an increase in mean column temperature, we find a similar pattern in the geopotential heights in the mid-troposphere (Z_{500}, Fig. 2b).

During the winter, differences in sea ice between the CTL and EXP are concentrated in the marginal sea ice zone with reductions of up to 100% sea ice cover (Fig. 1b). The local response to sea ice loss can be clearly seen in the surface fluxes and SLP. Over the marginal seas where sea ice loss is greatest and the atmosphere is exposed to more open ocean, there is a substantial increase in turbulent heat flux (defined as the sum of the sensible and latent heat flux) from the ocean to the atmosphere (Fig. 2f). Over the Bering/Beaufort Sea and Hudson Bay this change in turbulent heat flux reaches 100 $\mathrm{W\,m^{-2}}$. Consistent with a large decrease in surface albedo with a greater fraction of ice free ocean there is a large increase in net absorbed shortwave radiation at the surface with sea ice loss (Fig. 2h). The warmer surface temperatures of an ice free ocean, are associated with a larger net surface outgoing longwave radiation (Fig. 2g). Finally, there is a local reduction in SLP concentrated near regions of sea ice loss (Fig. 1e) consistent with a thermal low response (Fig. 2e). For example, over the Hudson Bay there are large negative SLP anomalies that reach -5 hPa. Over and downstream of these regions of newly open ocean in the Bering/Beaufort Seas and Hudson Bay there is enhanced total cloud cover (Fig. 2i) and precipitation ((Fig. 2f,j) consistent with enhanced sensible and latent heat flux associated with a transition to ice free conditions (Fig. 2f).

In the mid-latitudes, negative anomalies in the winter mean Z_{500} and SLP response indicate a deepening of the Aleutian low in the North Pacific (Fig. 2b,e). This is dynamically consistent with an intensification and elongation of the Pacific jet, where we would expect a corresponding eastward displacement of an enhanced secondary circulation favoring a more intense troposphere-deep cyclonic circulation. Here we identify the jet using the wind speed on the dynamic tropopause, where the dynamic tropopause is defined as the 2 potential vorticity unit (PVU; 1 PVU=$10^{-6}\mathrm{K\,kg^{-1}\,m^{-2}\,s^{-1}}$) surface (Fig. 2c). The dynamic tropopause is an ideal surface upon which to examine mid-latitude jets as this is where the jet is maximized and it rises with the increasing column temperature (Hoskins et al. 1985) thus ensuring that the differences are due to changes in the jet rather than the height of the tropopause. Coinciding with the elongated North Pacific jet and deeper Aleutian low, we see an increase in precipitation that extends to the west coast of North America (Fig. 2j).

Over the Atlantic, the response to sea ice loss includes an increase in Z_{500} (Fig. 2b) over Greenland and an equatorward shift of the North Atlantic jet, as seen in the dipole of wind speed on the dynamic tropopause (Fig. 2c), consistent with several previous studies (Deser et al. 2015; Sun et al. 2015; Blackport and Kushner 2017, 2018; Screen et al. 2018; Ronalds et al. 2020). Furthermore, we find a dipole in precipitation over the North Atlantic as would be expected from an equatorward shift of the storm track along with the jet (Fig. 2j). The winter mean SLP response shows no clear change in the Icelandic Low (Fig. 2e).

b. Identification of Large-Scale Patterns

To understand the impact of sea ice loss on LSMPs, we begin by first identifying dominant large-scale patterns of Z'_{500} using SOM (Fig. 3). Fig. 3 shows the Z'_{500} SOM nodes (LSMPs) in color and composites of Z_{500} in the control simulation (S_{CTL}) in black lines. In general, LSMPs on the left side of the SOM have amplified climatological ridges (troughs) over western (eastern) North America and vice versa on the right side of the SOM. Enhancement of the ridge/trough patterns shifts from being further east in LSMPs at the top of the SOM (e.g. LSMP [1,1]) to further west at the bottom (e.g. LSMP [5,1]). Similarly, negative (positive) anomalies over the climatological ridge (trough) shift from being to the west in LSMP [1,3] to further east in LSMP [5,3].

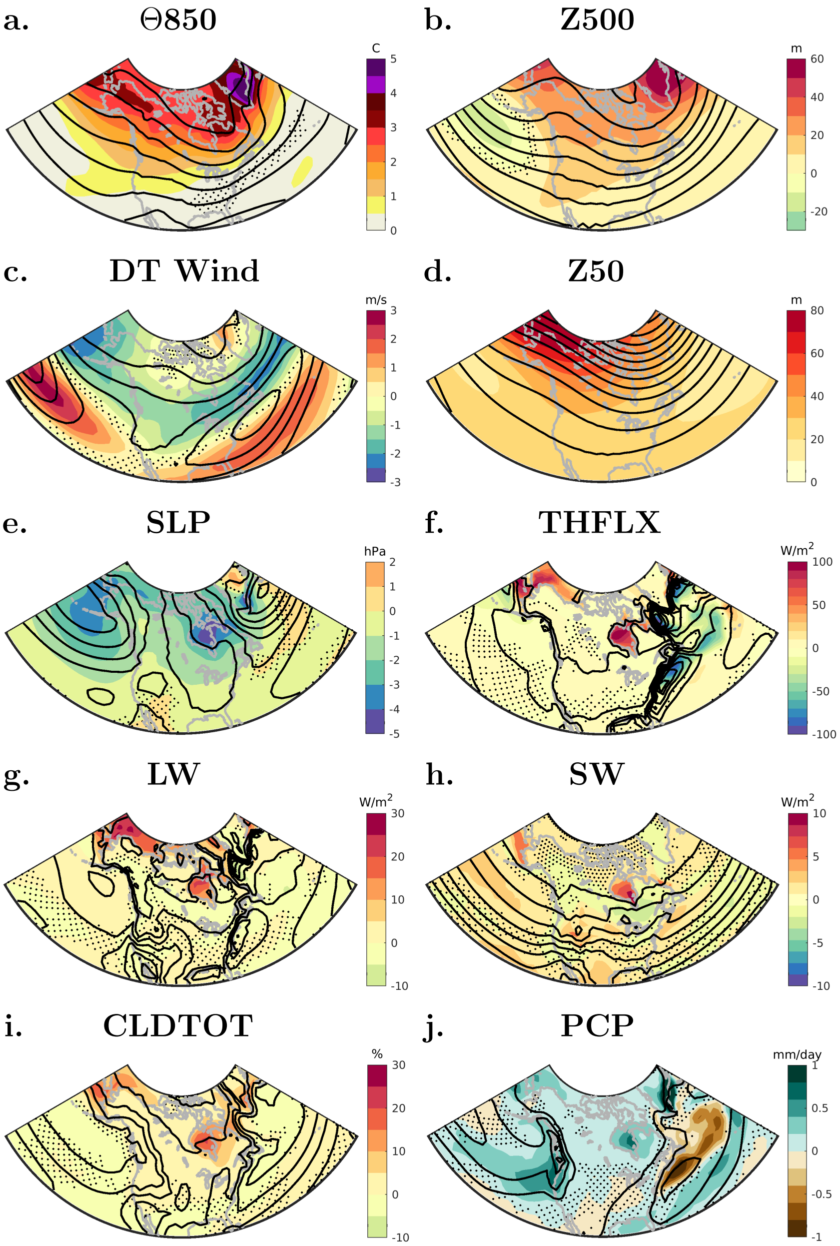

FIG. 2. Mean winter differences between simulations (EXP - CTL) in color and climatology in black contours for a) Θ_{850} with climatology contoured every 5 K, b) Z_{500} with climatology contoured every 100 m, c) wind speed on the dynamic tropopause (DT WIND) with climatology contoured every 5 m/s, d) 50hPa geopotential height (Z_{50}) with climatology contoured every 100 m, e) SLP with climatology contoured every 4 hPa, f) turbulent heat flux (THFLX) with climatology contoured every 10 $\mathrm{W\,m\,s^{-2}}$, g) Surface longwave radiation (LW) with climatology contoured every 5 $\mathrm{W\,m\,s^{-2}}$, h) Surface shortwave radiation (SW) with climatology contoured every 2 $\mathrm{W\,m\,s^{-2}}$, i) Total cloud cover (CLDT) with climatology contoured every 5%, and j) Precipitation (PCP) with climatology contoured every 2 $\mathrm{mm\,d^{-1}}$. Insignificant differences at the 5% significance level according to a resampling test are stippled.

The LSMPs [1,1] and [2,1] in the upper left corner have a pattern similar to the positive phase of the Pacific North American Pattern (PNA, Wallace and Gutzler (1981)) with negative anomalies in the Pacific and Eastern North America and positive anomalies over Alaska / the Pacific Northwest. Conversely, LSMP [5,3] in the bottom right corner resembles the negative PNA. LSMPs [1,1], [1,2] and [1,3] include anomalies over the North Atlantic that are consistent with a negative Arctic Oscillation (AO,Thompson and Wallace (1998)) or North Atlantic Oscillation (NAO, Hurrell (1995)) like pattern. LSMPs [1,1] and [1,2] have positive Z'_{500} near Iceland while LSMP [1,3] has a center of action shifted further west. LSMPs [1,2] and [1,3] have negative anomalies over the subtropical North Atlantic. In contrast, LSMPs [3,2] and [4,2] have weak positive AO/NAO-like anomalies. Although the NAO is an important feature of the Northern Hemisphere climate variability and exerts an impact on North American weather, our SOM is trained with data over North America and therefore we expect variability over the North Atlantic will have a limited presence as compared to other sources. LSMPs [4,1] and [5,1] have a strong positive anomaly over Alaska that acts to amplify and shift the climatological ridge over the Rockies further east, while LSMPs [3,3], [4,3], and [5,3] have a negative anomaly over Alaska. LSMPs [1,1], [1,2], [2,1], and [2,2] exhibit a strengthened Aleutian Low, while LSMPs [4,3], [5,1], [5,2], and [5,3] exhibit a weakened Aleutian low. Nodes in the center of the SOM have weaker patterns overall.

To obtain further understanding of the synoptic conditions associated with each map LSMP and their sensible weather impacts, we compute control simulation composites (S_{CTL}) for additional variables. LSMPs in the top left of the SOM (namely LSMPs [1,1], [1,2], [2,1], [2,2]) have deeper Aleutian lows as shown in their sea level pressure anomalies (SLP$'$, Figs. 4, 5) consistent with the negative values in Z'_{500} SOM (Fig. 3). Those on the right side of the SOM (namely LSMPs [3,3], [4,3], [5,3]) have Aleutian Lows that are shifted further east toward the continent and coupled with a high over the subtropics (Fig. 4, 5). This high/low pressure couplet of SLP over the Gulf of Alaska and west coast of North America acts to generate westerly lower-tropospheric winds through geostrophic balance arguments. This in turn can act to enhance the transport of warm maritime air into the continent, which is seen in the positive Θ'_{850} values over western North America associated with these LSMPs (Fig. 4). LSMPs on the top and left side of the SOM are generally colder, specifically nodes [1,1], [1,2], [3,1], and [4,1]. These are associated with either an enhancement of the climatological high pressure and ridge over western North America (LSMPs [1,1], [2,1], [3,1],

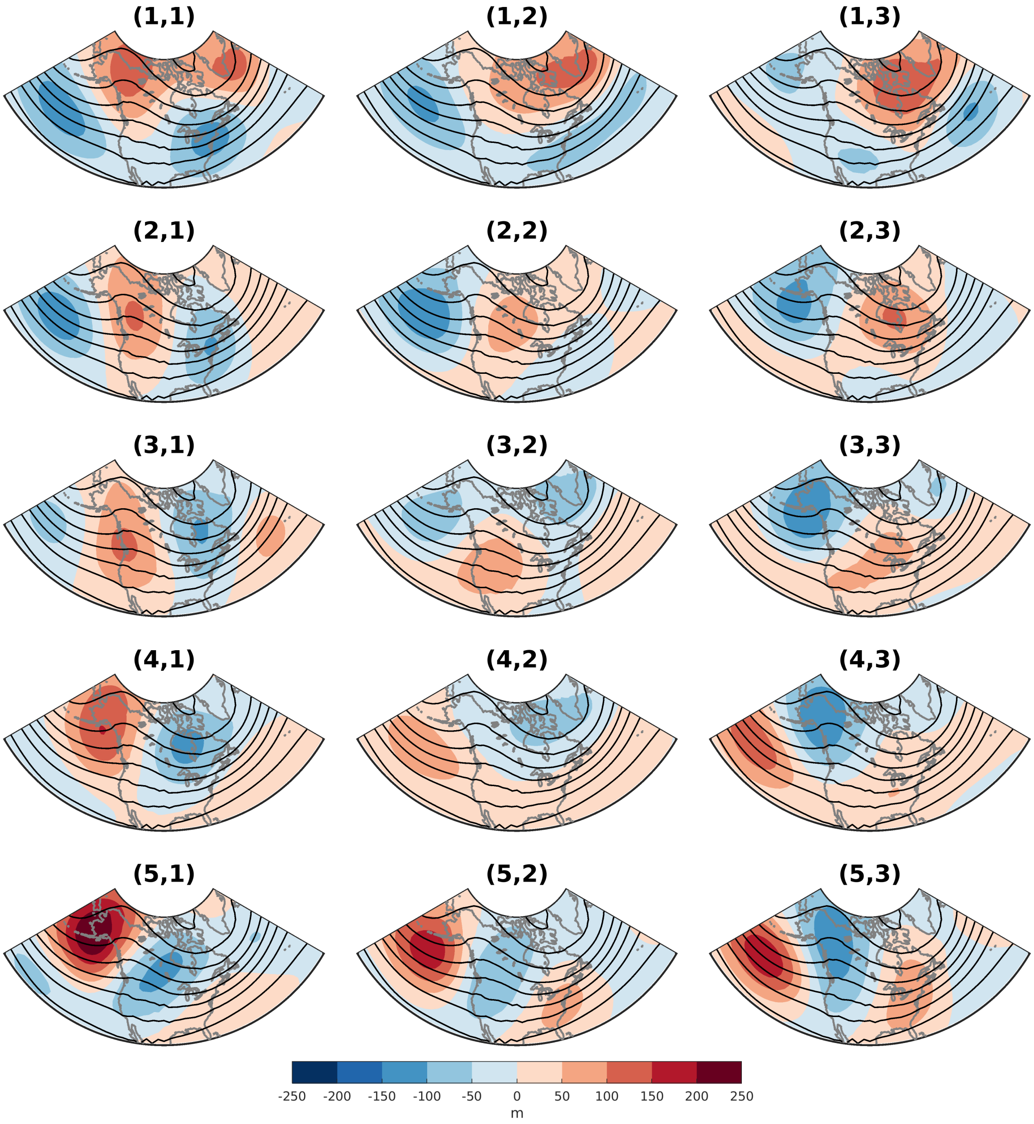

FIG. 3. SOM of DJF Z'_{500} (color, m) over North America with the DJF climatological mean Z_{500} (black contours every 100 m).

[4,1]) and/or a weakened Iceland Low (LSMPs [1,1] and [2,1]) consistent with the negative phase of the NAO (Fig. 4). LSMPs [1,2] and [4,1] are associated with particularly deep cold anomalies down to −2°C.

Circulation patterns can also play a key role in the precipitation over the continental US. LSMPs with strong Aleutian lows that are closer to the continent ([2,2], [2,3], [3,2], [3,3]) are associated with enhanced precipitation along the west coast whereas nodes with weaker Aleutian Lows ([4,1], [5,1], [4,2], [5,2]) have less precipitation along the west coast (Fig. 5 and contours in Fig. 9).

Enhanced precipitation in the Southeastern US is found in LSMPs [5,1], [5,2], [5,3] and [1,3], all of which are characterized by a trough over the Southeastern US (Fig. 5 and contours in Fig. 9). In contrast, precipitation is reduced in LSMPs [2,1], [3,1], and [3,2] where the trough is located offshore (Fig. 5 and contours in Fig. 9).

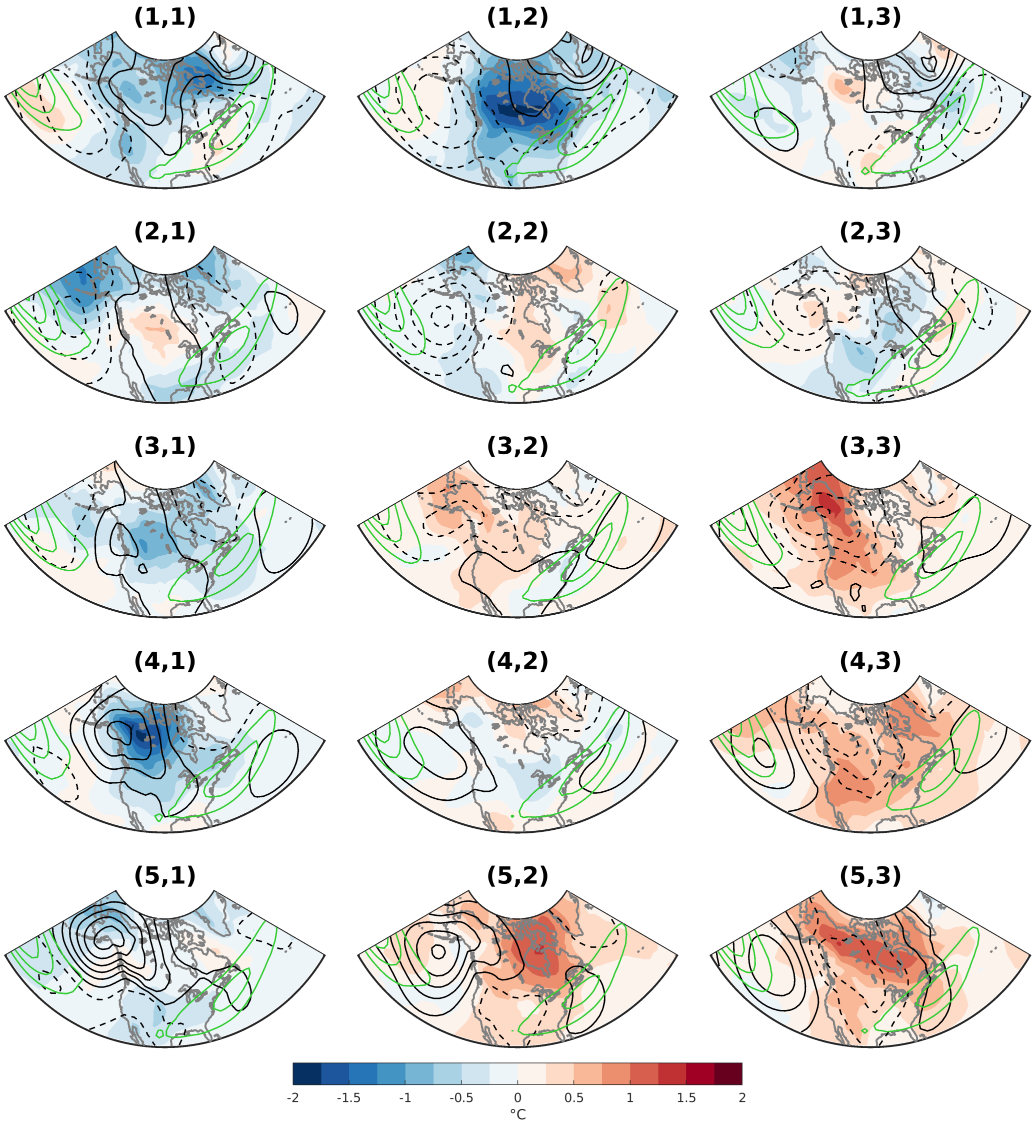

Fig. 4. CTL composites of Θ'_{850} (color, °C), SLP′ (black contours every 4 hPa, dashed negative from 2 hPa), and wind speed on the dynamic tropopause (green contours every 5 $\mathrm{m\,s^{-1}}$ from 35 $\mathrm{m\,s^{-1}}$)

Fig. 6a,b shows the associated frequency of each map node in the CTL and EXP simulations. All LSMPs in Fig. 3 are present in both the CTL and EXP simulations. In the CTL simulation, LSMPs [3,2], [4,2], and [4,3] occur most often. The LSMPs that occur least often are [1,1] and

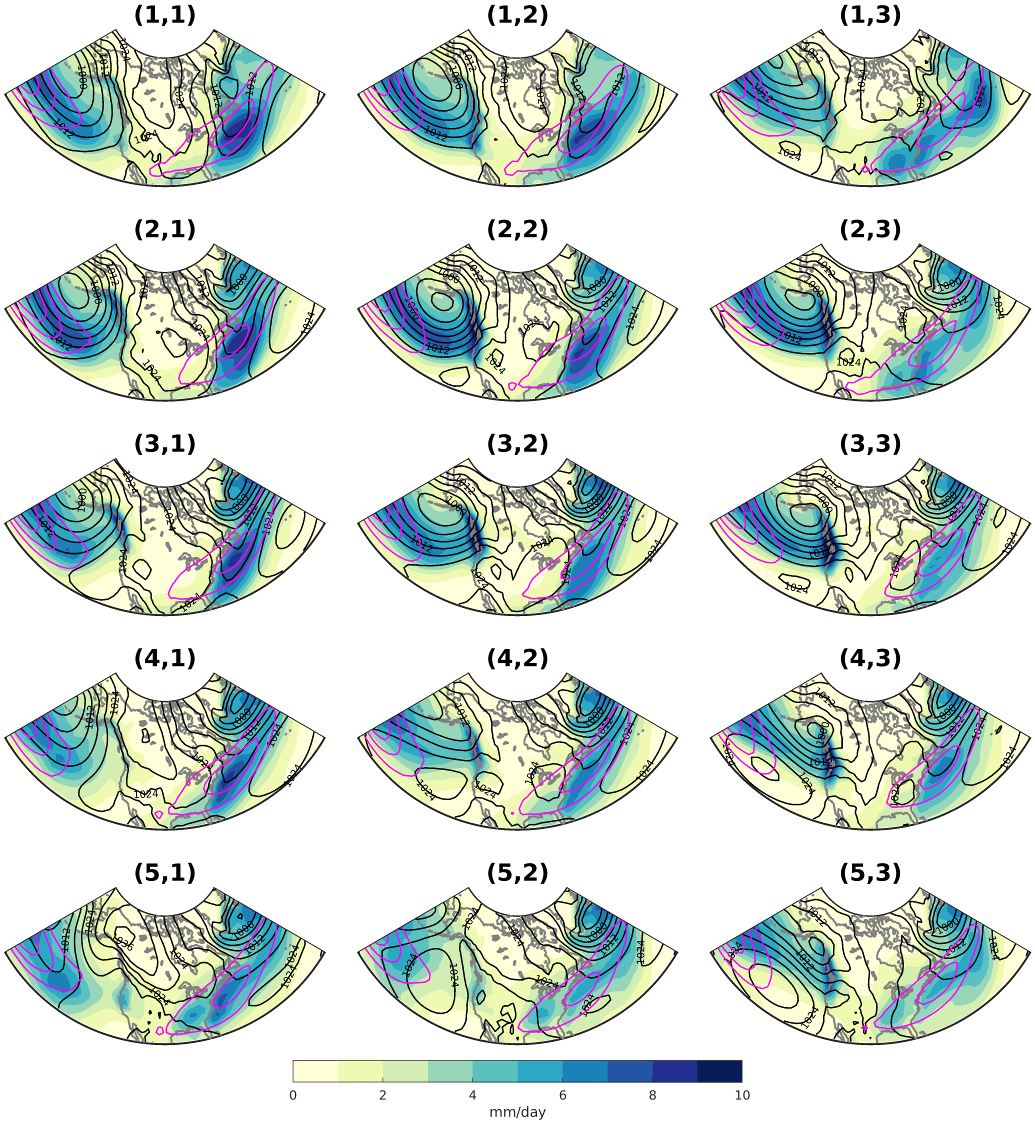

Fig. 5. CTL composites of total precipitation (color, $\mathrm{mm\,d^{-1}}$), SLP (black contours every 4 hPa), and wind speed on the dynamic tropopause (magenta contours every 5 $\mathrm{m\,s^{-1}}$ from 35 $\mathrm{m\,s^{-1}}$)

[1,2], both of which are characterized a deepened Aleutian low, cold Θ'_{850} over North America, and high SLP′ over northeastern Canada and Greenland. In the EXP simulation, LSMPs [2,2], [4,2], and [4,3] occur most often, while LMSPs [1,1], [2,1], and [3,1] occur least often. The mean residency time, defined as the number of consecutive days spent in a given map node, are shown in Fig. 6d,e for the CTL and EXP simulations respectively. Mean residency times range from 3.2-4.3 days with LSMP [5,1] having the highest and LSMP [4,2] the lowest residency time for both the CTL and EXP simulations. It should be noted that for both the frequency and residency time the

values will change depending on the SOM size (decreasing with increasing SOM size), therefore the actual values are less meaningful than how they might change between the CTL to the EXP simulations.

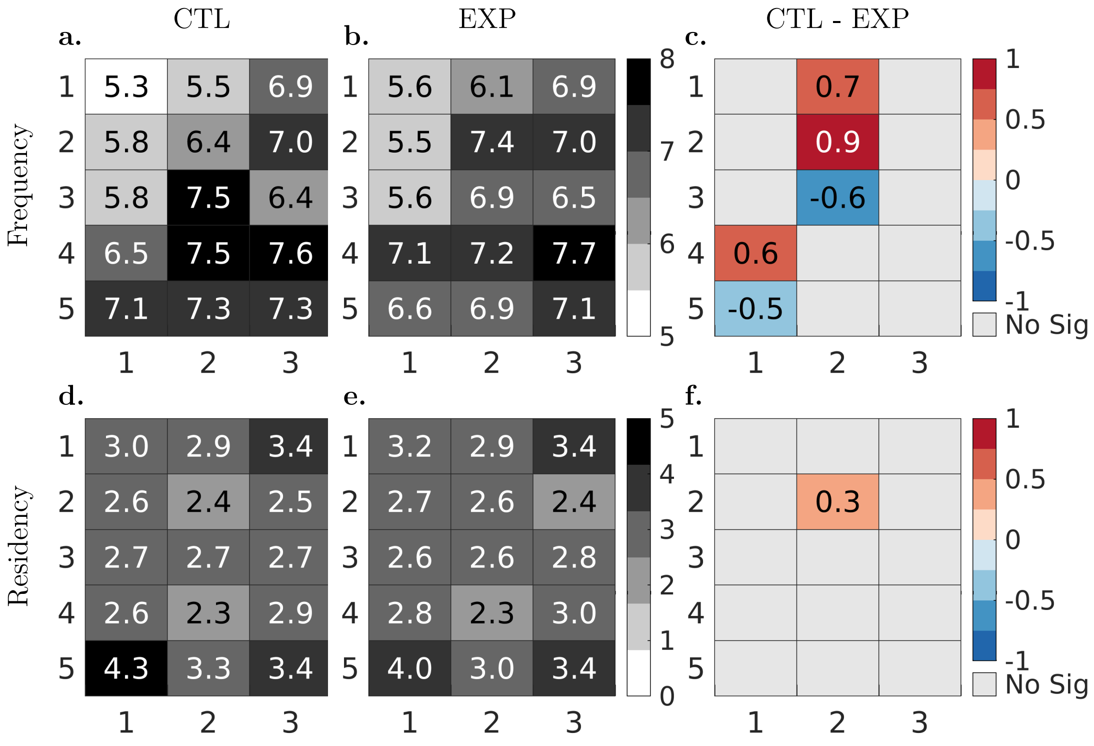

a.

	1	2	3
1	5.3	5.5	6.9
2	5.8	6.4	7.0
3	5.8	7.5	6.4
4	6.5	7.5	7.6
5	7.1	7.3	7.3

b.

	1	2	3
1	5.6	6.1	6.9
2	5.5	7.4	7.0
3	5.6	6.9	6.5
4	7.1	7.2	7.7
5	6.6	6.9	7.1

c.

	1	2	3
1		0.7	
2		0.9	
3		-0.6	
4	0.6		
5	-0.5		

d.

	1	2	3
1	3.0	2.9	3.4
2	2.6	2.4	2.5
3	2.7	2.7	2.7
4	2.6	2.3	2.9
5	4.3	3.3	3.4

e.

	1	2	3
1	3.2	2.9	3.4
2	2.7	2.6	2.4
3	2.6	2.6	2.8
4	2.8	2.3	3.0
5	4.0	3.0	3.4

f.

	1	2	3
1			
2		0.3	
3			
4			
5			

FIG. 6. Heatmaps of frequency of occurrence (top row) of each node in the CTL (a), EXP (b), and their difference (c) and mean residency time (bottow row) for each node in the CTL (d), EXP (e), and their difference (f). Differences are only shown when significant at the 95% level using a permutation test.

c. *Impact of Sea Ice Loss on LSMP Frequency and Residency*

To understand the impact of sea ice loss on LSMPs, we will first discuss the impact on their frequency of occurrence and residency. Fig. 6c demonstrates the difference in frequency of each LSMP between the CTL and EXP. LSMP [3,2] decreases in frequency by -0.6% while LSMPs [1,2] and [2,2] increase in frequency by 0.7% and 0.9% respectively. These changes may seem small; however, relative to the CTL frequency of 6.4% in LSMP [2,2], for example, the fractional increase is 14%. All of these LSMPs ([1,2], [2,2], and [3,2]) have anomalously strong Aleutian Lows but

LSMPs [1,2] and [2,2] are stronger than LSMP [1,3] (Figs. 3 and 4) therefore these changes in frequency imply that patterns with deepened Aleutian Lows become more common with sea ice loss. It should be noted that here we have already removed the seasonal mean difference between the experiments that was characterized by a mean deepening of the Aleutian Low and that this result shows further changes in how often these deepened Aleutian Low patterns occur. We also see that LSMP [5,1] decreases in frequency while LSMP [4,1] increases in frequency with sea ice loss. Since node [5,1] has a larger positive Z'_{500} over Alaska than node [4,1] (Fig. 3), this can be interpreted as the positive anomaly over Alaska becoming de-amplified.

Unlike the frequency, only LSMP [2,2] experiences a significant change in mean residency time, with an increase of 0.3 days. This LSMP also exhibited an increase in frequency, indicating that some of the increase in frequency is due to enhanced persistence. Since these LSMPs capture synoptic spatial scale variability, they include patterns associated with Rossby wave propagation across North America. The overall lack of change in residency times across the SOM implies that there is no general change in the speed of wave propagation owing to sea ice loss.

d. Impact of Sea Ice Loss on LSMP Pattern

To complete our investigation of sea ice impacts on LSMPs, we examine differences in LSMP composite mean (ΔS) for a variety of atmospheric variables. The impact of Arctic sea ice loss is to weaken the Z'_{500} in many LSMPs, which can be interpreted as a reduction in variability (Fig. 7). The best example of this is LSMP [1,2], where the magnitude of the gradient associated with the −NAO-like dipole in Z'_{500} between the Icelandic Low and Subtropical High is reduced by approximately 15% with sea ice loss. In many cases, the ΔS of Z'_{500} are not centered on the CTL composites Z'_{500} and thus are better characterized as a shift in location, for example the anomalous ridging along the west coast in LSMPs [4,1], [5,1], and [5,2] is shifted further south. A few LSMPs are amplified with sea ice loss, for example, the positive Z'_{500} in the subtropical Pacific in LSMPs [4,3] and [5,3] are deepened and in [5,3] extended further east toward the continent. LSMP [1,3] also has negative ΔS of Z'_{500} in the North Pacific consistent with a deepened Aleutian Low. In all cases, the ΔS of Z'_{500} are smaller than the CTL composites and so there is no change in the sign of the patterns. This is necessarily true for Z'_{500} since the SOM is trained and BMUs are assigned based on this field. However, for other fields, LSMP composites may see larger changes if the conditions associated with these Z'_{500} patterns change.

To understand the impact of sea ice loss on the sensible weather associated with these circulation patterns, we examine ΔS of Θ'_{850} (Fig. 8) and precipitation anomalies (Fig. 9). The most striking impact of sea ice loss on Θ'_{850} is in LSMP [1,2] (Fig. 8). This LSMP was associated with deep cold anomalies up to -1.75°C in the CTL simulation. However, the impact of sea ice loss far exceeds this at up to +4°C in ΔS of Θ'_{850}, resulting in a change in sign of Θ'_{850} associated with this LSMP in the CTL relative to the EXP. LSMP [4,1] that is also associated with strong cold anomalies over North America reaching -2°C in the CTL simulation experiences a large decrease in magnitude with sea ice loss of up to +1.5°C. Both LSMPs [4,1] and [1,2] increase in frequency with sea ice loss, so the circulation patterns typically associated with deep cold anomalies become more common with sea ice loss; however, they are much less cold or, in the case of [1,2], now associated with a warm Θ'_{850}.

Looking across the entire SOM, we see that a reduction in the amplitude of Θ'_{850} associated with these Z'_{500} LSMPs is ubiquitous (Fig. 8). Other LSMPs associated with large cold anomalies (LSMPs [1,1], [2,1], [5,1], and [2,3]) become warmer and those associated with warmer anomalies become colder. Several of these LSMPs (namely [3,3], [4,3], [5,3]), are not associated with significant changes in frequency (Fig. 6), so their contribution to changes in variability is solely through a change in pattern. This de-amplification of Θ'_{850} is consistent with the general reduction in Z'_{500} across the SOM owing to sea ice loss. One explanation is that the reduction of horizontal temperature gradients owing to AA may lead to a reduction in anomalous temperature advections occurring in these nodes, even though the mean impact of AA is already removed by virtue of computing the anomalies. This can result in reduced Θ'_{850} and through hypsometric arguments in a corresponding reduction in Z'_{500}.

The impact of sea ice loss on precipitation anomalies associated with these LSMPs is less robust and more localized (Fig. 9). LSMPs [3,1], [4,1], and [4,2] all experience a small decrease in precipitation along the California coast, acting to amplify the precipitation anomalies values typically associated with these LSMPs (Fig. 9). This is consistent with a positive SLP′ that acts to further reduce the transport of moist air to the region (Fig. S2). The opposite is true for LSMPs [1,1] and [2,2] (Fig. 9, S2). LSMP [1,3] experiences an increase in ΔS of precipitation anomalies in the southeastern US (Fig. 9) consistent with the enhanced troughing (Fig. 7, S2) occurring in proximity to the Gulf of Mexico and Atlantic Basin, well known moisture sources for the region. The opposite is true for LSMP [3,3].

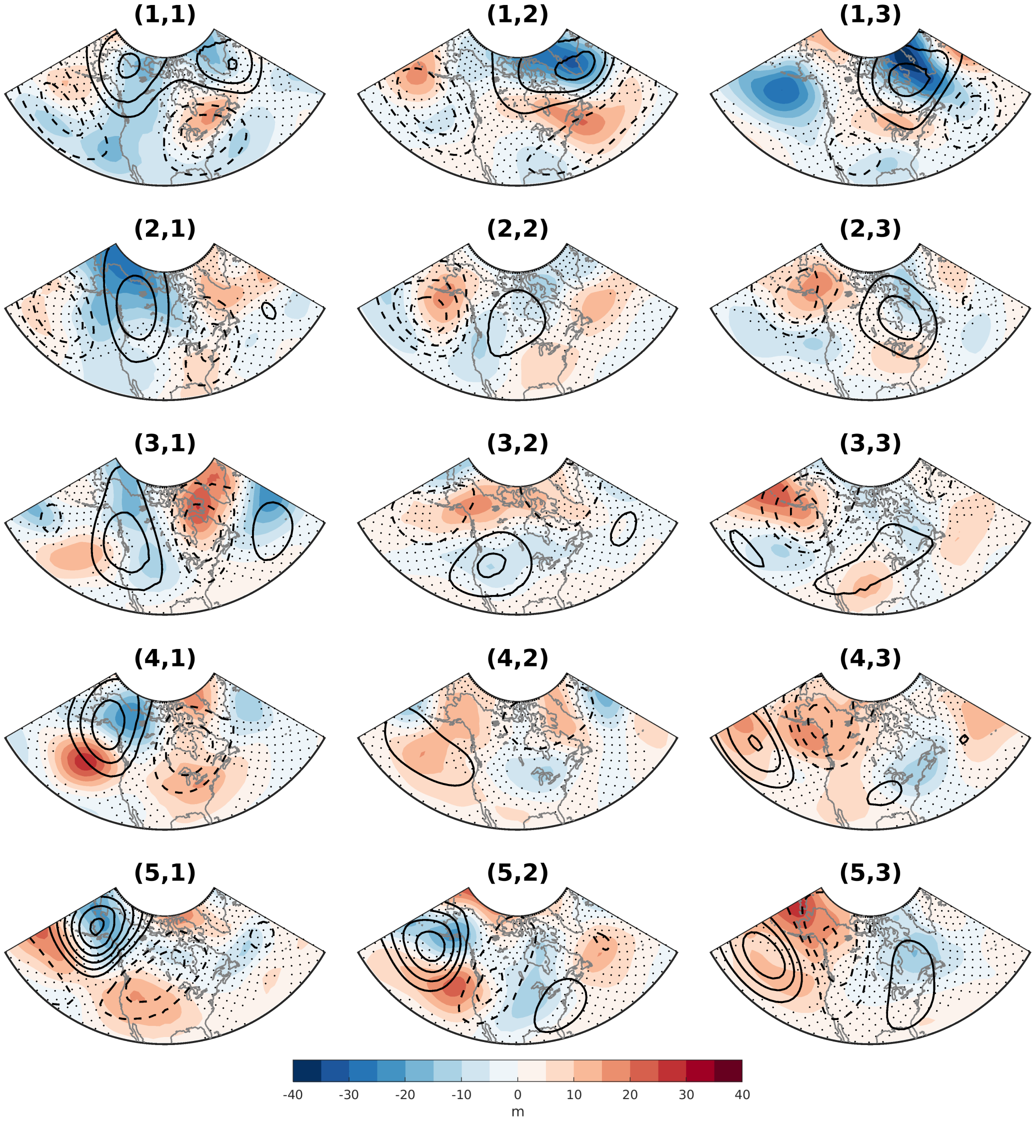

FIG. 7. CTL Composites of Z'_{500} (contours, every 50 m from ±50 m, dashed negative) and difference in composites (EXP-CTL) of Z'_{500} (color, stippled insignificant using Student's t-test).

e. Mechanisms Responsible for LSMP [1,2] Pattern Changes

Given the striking changes in LSMP [1,2] and in particular the associated Θ'_{850}, a deeper investigation into mechanisms operating in this node is warranted. First, it is important to recognize

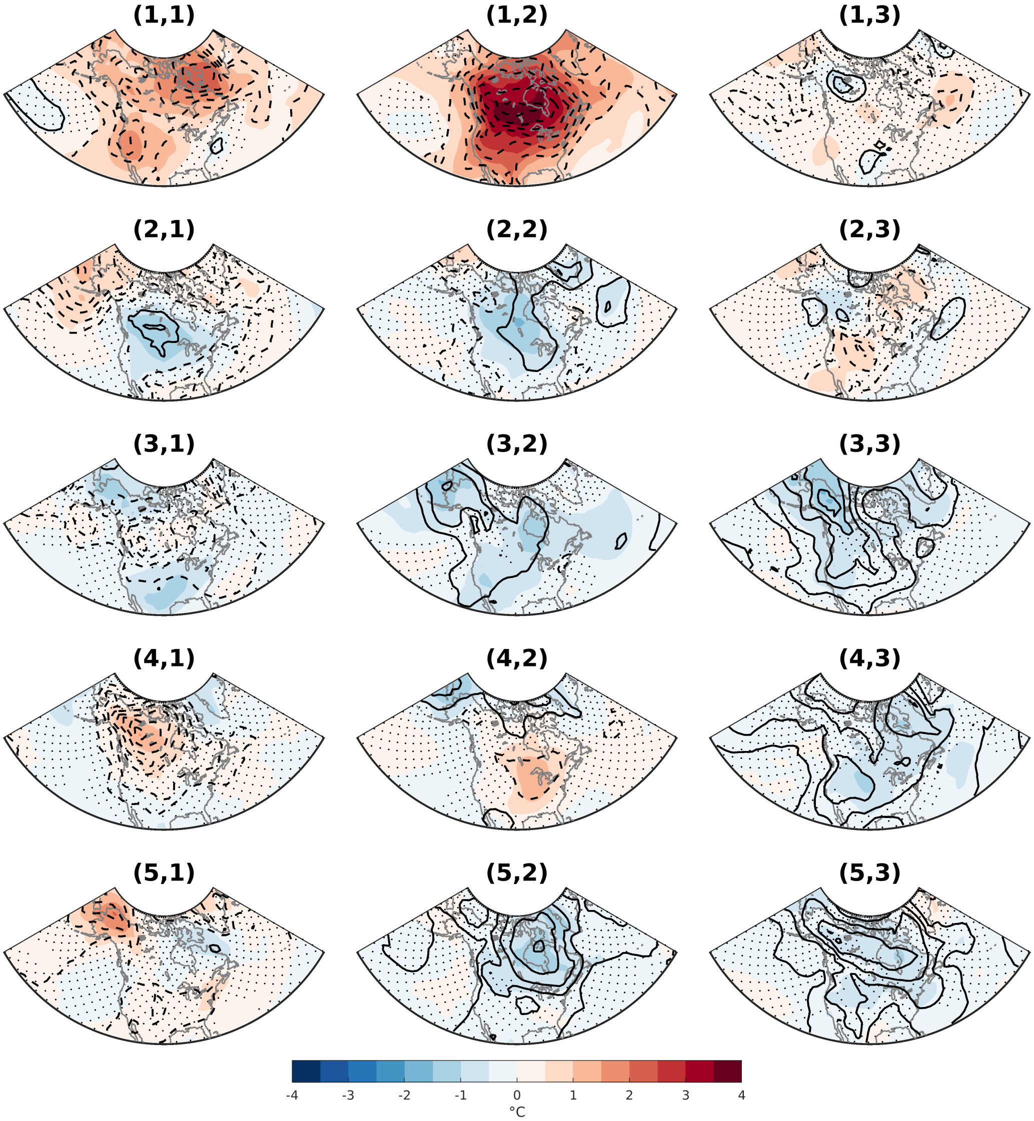

FIG. 8. CTL Composites of Θ'_{850} (contours, every 0.25° C from ±0.25° C, dashed negative) and difference in composites (EXP-CTL) of Θ'_{850} (color, stippled insignificant using Student's t-test).

that the LSMPs identified in this study are from anomalous Z_{500} fields relative to the respective climatologies of each simulation (i.e. Z'_{500}). Thus, these patterns represent atmospheric variability separate from mean impacts of sea ice loss. However, when it comes to understanding the impacts of these LSMPs on fields such as Θ_{850}, the mean impacts of sea ice loss can still be important. As such, in the ensuing analysis we will be examining both composites of total fields (e.g. Z_{500}) and anomaly fields (e.g. Z'_{500}).

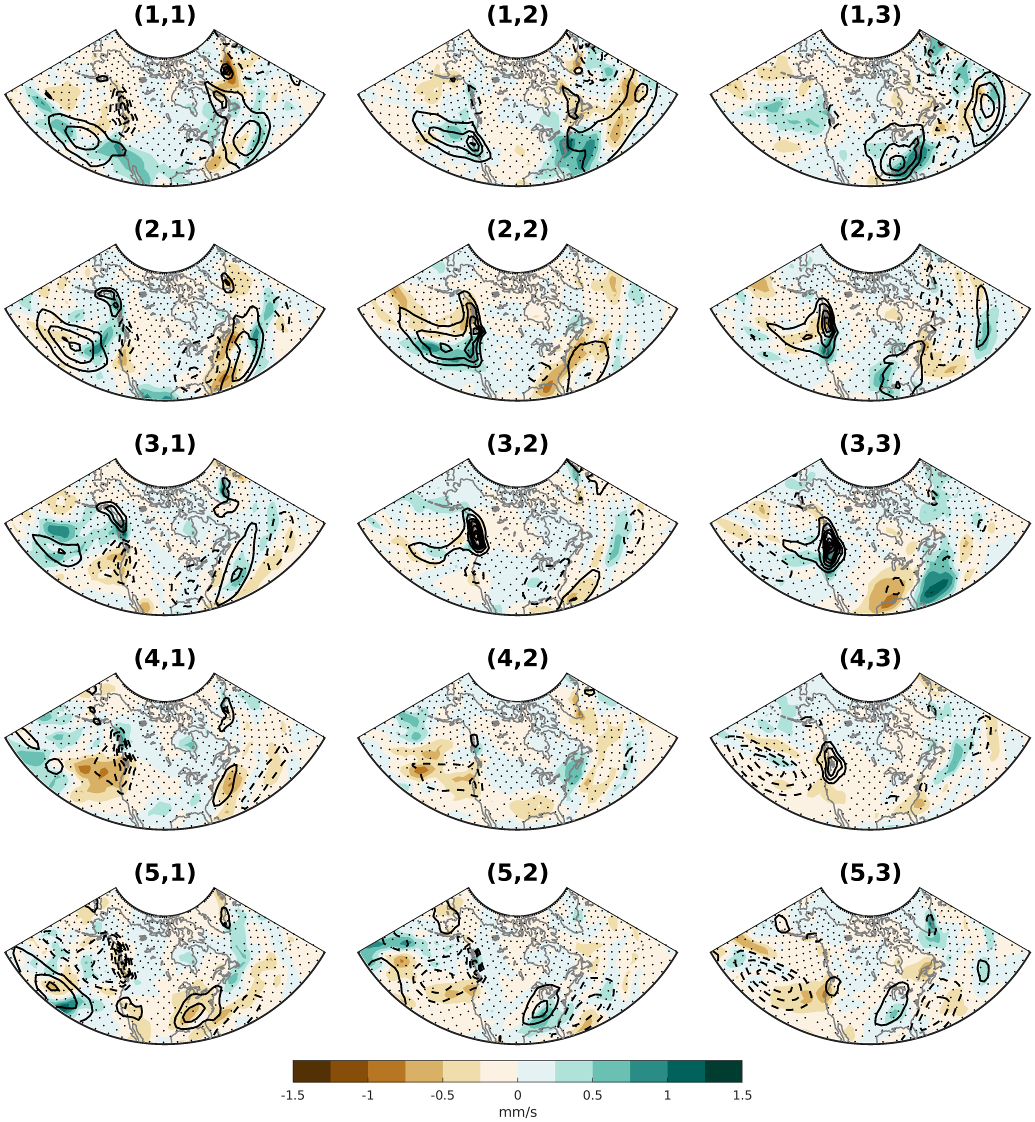

FIG. 9. CTL Composites of precipitation anomalies (contours, every $1\,\mathrm{mm\,d^{-1}}$ from $\pm 1\,\mathrm{mm\,d^{-1}}$, dashed negative) and difference in composites (EXP-CTL) of precipitation anomalies (color, stippled insignificant using Student's t-test).

Fig. 10 shows the CTL and EXP composite of Θ_{850} and SLP. In the CTL simulation, high SLP over the center of the continent and low SLP over the North Atlantic implies a north-northeasterly geostrophic wind. Coupled with the strong meridional background temperature gradient between the pole and the midlatitudes, there is implied geostrophic cold air advection over northeastern North America. Furthermore, the anticyclonic circulation around the high pressure system would aid in transporting this cold air throughout North America. This helps explain why LSMP [1,2] is associated with deep cold continental temperatures.

In the EXP simulations, the background temperature gradient from equator to pole is weakened, as is expected with AA (Fig. 10). This in and of itself would cause a reduction in cold air advection in this LSMP. However, we also see that the high pressure over Hudson Bay is weakened resulting in a slackening of the SLP gradient over eastern Canada and a weakening of the implied north-northeasterly geostrophic wind by roughly 30%. Furthermore, the overall reduction in the strength of the high pressure system would reduce the typical transport of this cold air into the interior of North America. This can be seen, for example, in the slacking of the meridional pressure gradient from Hudson Bay to the Gulf of Mexico coast. Therefore, though we could ascribe the changes in cold air advection to mean AA and the weakened temperature gradient (a thermodynamic impact), these changes in SLP also imply a large role for dynamical impacts.

As discussed previously, there is an increase in mean winter turbulent heat flux and decrease in mean winter SLP between the two simulations over Hudson Bay (Fig. 2), consistent with a local thermal low pressure response to sea ice loss. The difference in CTL and EXP LSMP [1,2] composites of SLP′ are insignificant over much of the North American continent (Fig. 11c). Furthermore, the effect of turbulent heat flux is smaller in LSMP [1,2] (Fig. 11d) potentially owing to the warmer Θ'_{850} reducing the ocean-atmosphere temperature gradients (Fig. 11a). This implies that much of the differences in the SLP gradients discussed above are owing to differences in the mean climatology between the CTL and EXP simulations and how this projects onto the LSMP [1,2] circulation pattern rather than changes in SLP that are specific to this LSMP. For this node in particular, where the high pressure in this region is an important factor, this mean change acts to reduce the zonal SLP gradient and consequently the strong cold air advection in northeastern North America that characterizes the LSMP.

In addition to changes in temperature advection, diabatic processes may also play a role in the increased Θ'_{850} associated with LMSP [1,2]. There is an increase in total cloud cover anomalies and precipitation anomalies downstream (south) of Hudson Bay with sea ice loss (Fig. 11e,f). This is expected given the mean increase in moisture and heat flux (Fig. 2f) from the ice-free surface with sea ice loss (Fig. 1b). This increase in clouds and precipitation relative to other LSMPs is associated with less incoming net short wave radiation and less upward longwave radiation (Fig.

11g,h). Furthermore, we would expect an increase in diabatic heating to be associated with cloud and precipitation generation, though this cannot be directly confirmed with the variables saved in these model simulations. These results imply a role of diabatic processes in addition to temperature advection in producing the large differences in Θ'_{850} in LSMP [1,2].

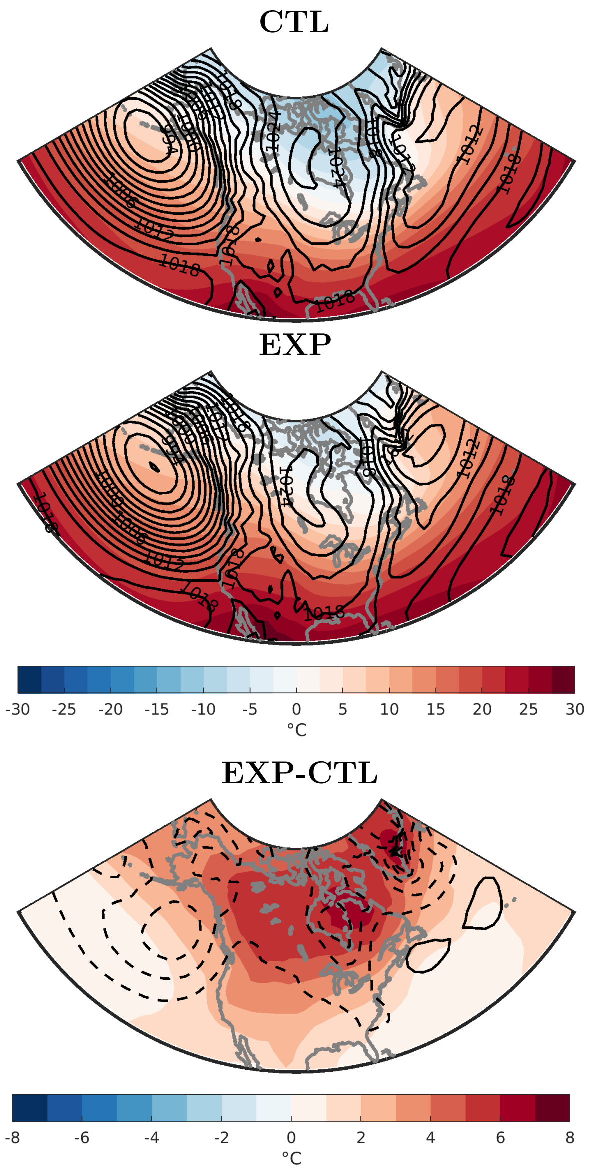

Fig. 10. Node [1,2] composites of Θ_{850} (color) and SLP (black contours every 4hPa) for a) CTL, b) EXP and c) their difference (EXP - CTL). For a) and b) SLP contours are every 4hPa and for c) SLP contours are every 1hPa with dashed negative values and the 0 contour omitted.

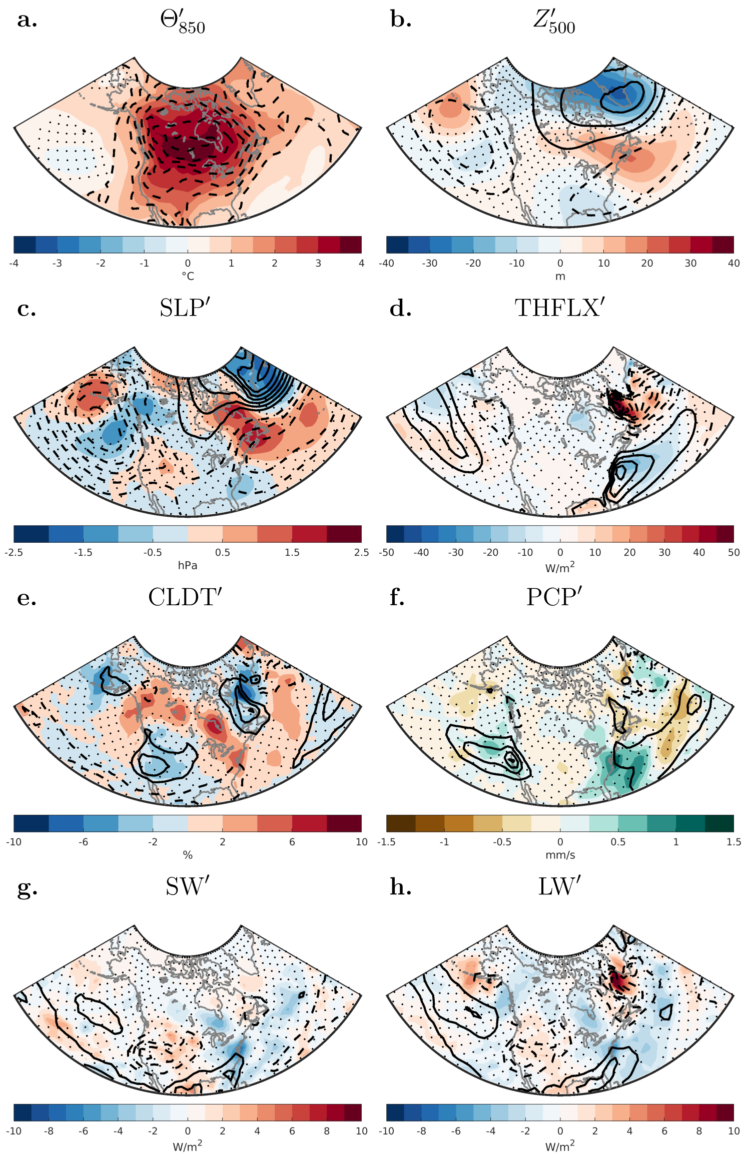

FIG. 11. Node [1,2] CTL composites (contours) and differences (EXP-CTL) in composites (color) for a) Θ'_{850} (contours every 0.25° C from ±0.25° C, dashed negative), b) Z'_{500} (contours every 50 m from ±50 m, dashed negative), c) SLP′ (contours every 2 hPa from ±2 hPa, dashed negative),d) turbulent heat flux anomalies (THFLX′, contours every 20 $\mathrm{W\,m\,s^{-2}}$ from ±20 $\mathrm{W\,m\,s^{-2}}$, dashed negative), e) total cloud cover anomalies (CLDT′, contours every 5% from ±5%, dashed negative), f) precipitation anomalies (PCP′, contours every $1\mathrm{mm\,d^{-1}}$ from $\pm 1\mathrm{mm\,d^{-1}}$, dashed negative), g) incoming shortwave radiation anomalies (SW′, positive down, contours every 5 $\mathrm{W\,m\,s^{-2}}$ from $\pm 5\mathrm{W\,m\,s^{-2}}$, dashed negative), and h) outgoing longwave radiation anomalies (LW′, positive up, contours every 5 $\mathrm{W\,m\,s^{-2}}$ from $\pm 5\mathrm{W\,m\,s^{-2}}$, dashed negative) . All figures have insignificant differences at the 5% level computed using a Student's t-test stippled.

f. Contributions of changes in LSMPs to mean DJF response to sea ice loss

AA is one of the most notable impacts of Arctic sea ice loss. In Fig. 2a we can see this reflected in the DJF seasonal mean difference between the CTL and EXP ($\Delta\Theta_{850}$). As described above, some LSMPs are associated with greater changes Θ'_{850} than others (e.g. LSMP [1,2]). Decomposing the DJF mean Θ'_{850} response by LSMP contribution can provide an avenue into better understanding of how synoptic scale processes relate to mean Θ'_{850} response and elucidate additional mechanisms responsible for AA that might otherwise be obscured.

As discussed in the methods section, the mean difference between experiments can be approximated as those arising due to changes in frequency versus pattern of the LSMPs (Eqn. 4). For Θ_{850} the contribution from changes in frequency are much smaller than from changes in pattern (not shown). On the left side of equation 4, $\Delta(fS)$ is an approximation of the seasonal mean difference between experiments for a given variable (e.g. $\Delta\Theta_{850}$). Substituting these assumptions, we can re-write equation 4 for Θ_{850} as:

$$\Delta\Theta_{850} \approx \sum_{i=1}^{n} f_{avg,i}\Delta S_i \tag{8}$$

where $f_{avg,i}$ is the mean frequency of occurrence over the CTL and EXP simulations and ΔS_i is the composite mean Θ_{850} of EXP minus that of CTL for a given node i. Expanding out the summation, dividing both sides by $\Delta\Theta_{850}$ and multiplying by 100 we can obtain the percent contribution of each node to $\Delta\Theta_{850}$.

$$100 \approx \frac{f_{avg,1}\Delta S_1}{\Delta\Theta_{850}} \cdot 100 + \frac{f_{avg,2}\Delta S_2}{\Delta\Theta_{850}} \cdot 100 + \ldots + \frac{f_{avg,15}\Delta S_{15}}{\Delta\Theta_{850}} \cdot 100 \tag{9}$$

In Fig. 12, each of the terms of the right hand side are plotted, showing the percent contribution of each node to the mean DJF Θ_{850} response. The sum of all the percent contributions over all nodes is approximately equal to 100 (±5%) at each grid point location, confirming that changes in composite are indeed the greatest contributor to the mean Θ_{850} response.

To avoid the creation of artificially high values of percent contribution where $\Delta\Theta_{850}$ is very small, grid points where $\Delta\Theta_{850}$ is not statistically significant are masked out in Fig. 12. This is computed using a permutation test applied at each grid point to determine if the mean of DJF days used for the SOM analysis in the CTL are different from the EXP simulation with a significance level of 95%. This is similar to test used in Fig. 2 except there the DJF seasonal mean is computed first and the null hypothesis is that the seasonal means are the same.

If each of these nodes contributed equally to the mean Θ_{850} response, we would expect the percent contribution over 15 nodes to be 6.6% at each grid point. To test this, we compute a null distribution of percent contributions using a permutation test. Here the percent contributions are computed as in equation 9 but using an average frequency of 6.6% and the number of days per composites equal to the frequency times the number of input data vectors. We then shuffle the SOM node labels and choose a new set of CTL and EXP randomly without replacement and compute the difference in their composites. This process is repeated 500 times and if the actual percent contribution to the mean Θ_{850} response is greater than the 97.5th or less than the 2.5th percentiles of this null distribution, it is considered significant at the 95% level.

The results show that there are indeed nodes that contribute much more significantly to mean Θ_{850} response than others. LSMP [1,2] stands out for its significant contributions to mean DJF Θ_{850} response over the majority of North America ranging from 20-50%. Over Northern Canada (including the Northwest Territories, Nunavut, and Northern Quebec) where mean Θ_{850} response is greatest, LSMP [1,2] contributes up to 20% of the total mean Θ_{850} response. This is more than double the rate if there was an equal distribution across nodes. LSMP [4,1] also has a notable increase in contribution to the mean Θ_{850} response of up to 15% over the Yukon and Northwest Territories. It should be noted that these two LSMP were associated with deep cold anomalies in the CTL simulations (Fig. 4) in these regions. This implies that processes specific to these LSMPs, such as those outlined in Section 3c, are important for creating the mean Θ_{850} response and can occur on synoptic time scales.

In the midlatitudes, the mean Θ_{850} response is much smaller and the contributions of LSMPs is larger. LSMP [1,2] contributes up to 50% to the mean Θ_{850} response in the southern United States. This implies that LSMP [1,2] plays an important role in propagating the mean Θ_{850} response into the mid-latitudes. There are also notable positive contributions to the mean Θ_{850} response in the southern United States from LSMPs [1,1], [2,3], and [4,2] as well as negative contribution other LSMPs including [2,1], [2,2], [3,1], [3,2], [3,3], [4,1], and [4,3]. This is consistent with the general reduction in intensity in Θ_{850} across LSMPs identified in Fig. 8. It should be noted that in these regions where $\Delta\Theta_{850}$ is smaller, the percent contribution will be much larger for the same ΔS_i.

One interpretation of these results is therefore that when the mean signal is smaller the impact of internal variability will be larger.

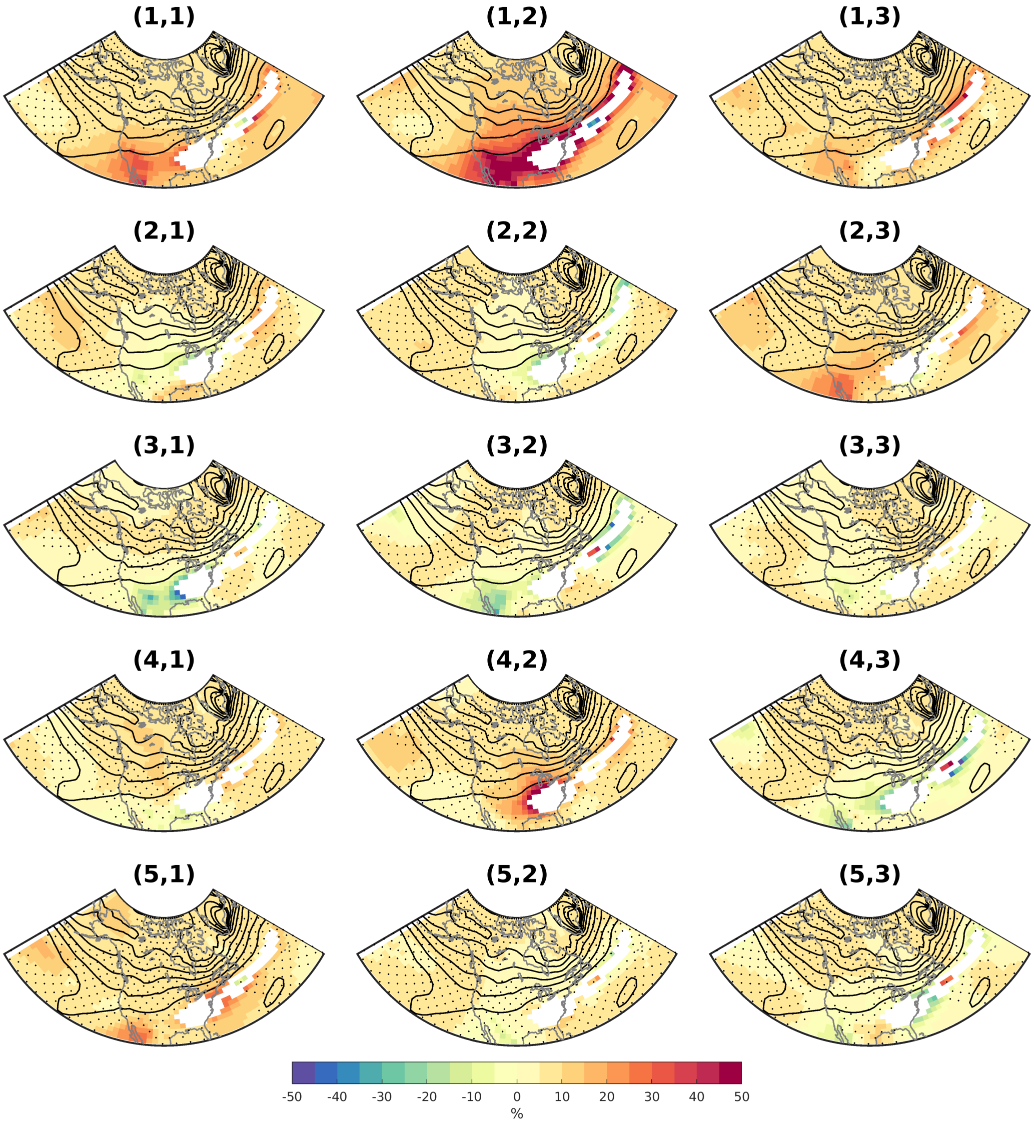

FIG. 12. Percent contribution of changes in each LSMP composite pattern to mean Θ_{850} in DJF (color). For reference, the DJF mean difference between CTL and EXP ($\Delta\Theta_{850}$) are provided in contours every $0.5°C$ beginning at $0.5°C$ as shown in Fig. 2a in color. Locations where $\Delta\Theta_{850}$ is not significantly different at the 95% confidence level as determined using a permutation test are masked out. Stippling shows regions were the percent contribution of changes in LSMP composite are not significant at a 95% level as determined using a permutation test.

4. Conclusions

The goal of this study was to identify the impact of future sea ice loss on large-scale meteorological patterns (LSMPs) and their associated sensible weather impacts. We analyze output from two fully-coupled CESM-WACCM simulations, one with sea ice nudged to the ensemble mean of the WACCM historical runs averaged over 1980-1999, and the other simulation nudged to projected RCP 8.5 values over 2080-2099. A machine learning method, self-organizing maps (SOMs), is used to identify LSMPs of anomalous 500 hPa in both experiments. Composite analysis of days assigned to these LSMPs is then used to understand the associated sensible weather conditions.

To identify the impact of sea ice loss on LSMPs, we quantify differences in how often these LSMPs occur (frequency) and for how many consecutive days data are classified in these LSMPs (residency). There are significant changes in LSMP frequency, most notably with two patterns associated with the coldest potential temperatures at 850 hPa (Θ_{850}) becoming more common in the future. However, there were little changes in the residency across the set of LSMPs, indicating that there is no general change in the speed of propagation of Rossby waves or stagnation of the flow with sea ice loss.

The impact of sea ice loss on LSMP patterns and their associated sensible weather impacts were identified by taking differences in composites of the CTL and EXP simulations for a variety of variables. In general, sea ice loss tends to de-amplify and in some cases shift the LSMP patterns, as seen in the composites differences in Z'_{500}. The impact of sea ice loss on Θ'_{850} is generally consistent with the general reduction in amplitude of the Z'_{500}. This is consistent with previous studies that suggested that decreases in the variance of temperature can occur due to the mean AA (Screen 2014; Screen et al. 2015; Collow et al. 2019; Dai and Deng 2021). Since the amplitude of tropospheric waves can generally be attributed to the displacement of air masses, it makes sense that with a reduction in the background temperature gradient associated with AA we would find a commensurate reduction in amplitude of LSMPs and their associated Θ'_{850}. There are less robust and more localized impacts of sea ice loss on precipitation anomalies associated with the LSMPs that are generally consistent with SLP′ changes.

One LSMP in particular, LSMP [1,2], exhibits a striking change in associated Θ'_{850} with sea ice loss. In the CTL simulation, this LSMP is associated with deep cold anomalies of Θ'_{850} reaching -1.75°C; however, with Arctic sea ice loss there is an increase in Θ'_{850} exceeding 4°C. LSMP [1,2] is associated with a ridge of higher pressure over the center of the continent that would facilitate Northerly flow of cold Arctic air deep into the continental US and Canada in the CTL simulation, as can be seen in the cold anomalies across much of the North American continent. AA reduces the meridional temperature gradient and thus would result in a reduction in cold air advection associated with this LSMP.

In this framework, it is possible to further identify the coincident impact of dynamical forcing. With Arctic sea ice loss, there are enhanced turbulent heat fluxes from the newly ice free Hudson Bay and the resulting local thermal low pressure anomaly in the wintertime. This results in both a reduction in the southward extent of the high SLP ridge and a weakening of the localized SLP gradient, consequently limiting the geostrophic meridional flow. Since these SLP changes are related to a local thermal response to sea ice loss that are geographically tied to Hudson Bay, they are likely robust to internal variability unlike many other dynamical impacts of sea ice loss. The combined impact of these two changes in the background mean state, both dynamical and thermodynamical, would result in a reduction in cold air advection. This analysis indicates that when it comes to the sensible weather impacts associated with LSMPs, there is an interplay between changes in the mean state and changes in the LSMP.

We further identify diabatic forcing mechanisms that may increase the Θ'_{850} in this LSMP. With Arctic sea ice loss, there is an increase in total cloud cover anomalies downstream of Hudson Bay with a coinciding decrease in anomalous shortwave radiation reaching the surface and increase in anomalous longwave radiation down. Along with this increase total cloud cover anomalies there is also an enhancement of precipitation anomalies, both of which are likely associated with latent heating although this cannot not be confirmed given the fields available in our simulations.

Given the association of LSMP [1,2] with large changes in Θ'_{850} owing to sea ice loss, a follow-on question was how important this specific LSMP is to the overall mean Θ_{850} response which is largely an AA signal. We find that in the Canadian north where the mean Θ_{850} response is large, this single LSMP accounts for up to 20% of the total signal. This is significantly larger than the 6.6% that would be expected if that signal were equally distributed among all the LSMPs. Although the mean Θ_{850} response is weaker in the midlatitudes, the role of LSMP [1,2] is even greater reaching 50% in the southern United States. This implies that LSMP [1,2] play an out-sized role in the mean Θ_{850} response and its propagation further south.

Although we haven't examined extreme temperature events in this study, LSMP [1,2] does resemble the broad-scale patterns associated with cold-air outbreaks over the Eastern US (e.g. Walsh et al. 2001). Previous literature has highlighted the role of AA in reducing the intensity of cold air outbreaks over North America (Screen et al. 2015; Ayarzagüena and Screen 2016); however, this analysis demonstrates that further investigation including the role of dynamics and diabatic effects in cold air outbreaks could yield new insight into the problem.

The results in this study demonstrate that there are notable changes in LSMPs and their associated sensible weather with Arctic sea ice loss. However, here we have shown results from just a single set of climate model simulations. Future work conducing a similar analysis with a suite of climate model experiments, such as those available in the Polar Amplification Model Intercomparison Project (PAMIP, Smith et al. (2019)), would help confirm the robustness of these results.

Acknowledgments. We would like to thank Kevin Bowley for insightful discussions regarding this research. This research was supported by NSF Grant AGS-2236771. NCAR is sponsored by the National Science Foundation under Cooperative Agreement 1852977. We would like to acknowledge high-performance computing support from Cheyenne (doi:10.5065/D6RX99HX) provided by NCAR's Computational and Information Systems Laboratory, sponsored by the National Science Foundation. Additional computations for this research were performed on the Pennsylvania State University's Institute for Computational and Data Sciences' Roar supercomputer.

Data availability statement. The WACCM simulations utilized in this study and the final SOM used to identify the LSMPs are openly available from the Penn State DataCommons at https://doi.org/10.26208/144H-0X26. The Self-Organizing Map Program Package (SOM_PAK; Kohonen (2001)) is available at http://www.cis.hut.fi/research/som-research/.

References

Alexander, M., U. S. Bhatt, J. Walsh, M. Timlin, J. Milller, and J. Scott, 2004: The Atmospheric Response to Realistic Arctic Sea Ice Anomalies in an AGCM during Winter. *Journal of Climate*, **17 (5)**, 890–905, URL https://doi.org/10.1175/1520-0442(2004)017⟨0890:TARTRA⟩2.0.CO;2.

Ayarzagüena, B., and J. A. Screen, 2016: Future Arctic sea ice loss reduces severity of cold air outbreaks in midlatitudes. *Geophysical Research Letters*, **43 (6)**, 2801–2809, https://doi.org/10.1002/2016GL068092.

Barnes, E. A., 2013: Revisiting the evidence linking Arctic amplification to extreme weather in midlatitudes. *Geophysical Research Letters*, **40 (17)**, 4734–4739, https://doi.org/10.1002/grl.50880.

Barnes, E. A., and J. A. Screen, 2015: The impact of Arctic warming on the midlatitude jet-stream: Can it? Has it? Will it? *Wiley Interdisciplinary Reviews: Climate Change*, **6 (3)**, 277–286, https://doi.org/10.1002/wcc.337.

Blackport, R., and P. J. Kushner, 2017: Isolating the atmospheric circulation response to arctic sea ice loss in the coupled climate system. *Journal of Climate*, **30 (6)**, 2163–2185, https://doi.org/10.1175/JCLI-D-16-0257.1.

Blackport, R., and P. J. Kushner, 2018: The role of extratropical ocean warming in the coupled climate response to Arctic sea ice loss. *Journal of Climate*, **31 (22)**, https://doi.org/10.1175/JCLI-D-18-0192.1.

Blackport, R., and J. A. Screen, 2020: Insignificant effect of Arctic amplification on the amplitude of midlatitude atmospheric waves. *Science Advances*, **6 (8)**, 1–10, https://doi.org/10.1126/sciadv.aay2880.

Cattiaux, J., Y. Peings, D. Saint-Martin, N. Trou-Kechout, and S. J. Vavrus, 2016: Sinuosity of midlatitude atmospheric flow in a warming world. *Geophysical Research Letters*, **43 (15)**, 8259–8268, https://doi.org/10.1002/2016GL070309.

Cohen, J., and Coauthors, 2014: Recent Arctic amplification and extreme mid-latitude weather. *Nature Geoscience*, **7 (9)**, https://doi.org/10.1038/ngeo2234.

Collow, T. W., W. Wang, and A. Kumar, 2019: Reduction in Northern Midlatitude 2-m Temperature Variability due to Arctic Sea Ice Loss. *Journal of Climate*, **32 (16)**, 5021–5035, https://doi.org/10.1175/JCLI-D-18-0692.1.

Comiso, J. C., W. N. Meier, and R. Gersten, 2017: Variability and trends in the Arctic Sea ice cover: Results from different techniques. *Journal of Geophysical Research: Oceans*, **122 (8)**, 6883–6900, https://doi.org/10.1002/2017JC012768.

Dai, A., and J. Deng, 2021: Arctic amplification weakens the variability of daily temperatures over northern middle-high latitudes. *Journal of Climate*, **34 (7)**, 2591–2609, https://doi.org/10.1175/JCLI-D-20-0514.1.

Dai, A., D. Luo, M. Song, and J. Liu, 2019: Arctic amplification is caused by sea-ice loss under increasing CO2. *Nature Communications*, **10 (121)**, https://doi.org/10.1038/s41467-018-07954-9.

Deser, C., R. Tomas, M. Alexander, and D. Lawrence, 2010: The Seasonal Atmospheric Response to Projected Arctic Sea Ice Loss in the Late Twenty-First Century. *Journal of Climate*, **23 (2)**, 333–351, https://doi.org/10.1175/2009JCLI3053.1, URL http://journals.ametsoc.org/doi/abs/10.1175/2009JCLI3053.1.

Deser, C., R. a. Tomas, and L. Sun, 2015: The role of ocean-atmosphere coupling in the zonal mean atmospheric response to Arctic sea ice loss. *Journal of Climate*, **28**, 2168–2186, https://doi.org/10.1175/JCLI-D-14-00325.1, URL http://journals.ametsoc.org/doi/abs/10.1175/JCLI-D-14-00325.1.

Francis, J., and S. Vavrus, 2012: Evidence linking Arctic amplification to extreme weather in mid-latitudes. *Geophysical Research Letters*, **39 (6)**, 1–6, https://doi.org/10.1029/2012GL051000, URL http://doi.wiley.com/10.1029/2012GL051000.

Francis, J. A., and S. J. Vavrus, 2015: Evidence for a wavier jet stream in response to rapid Arctic warming. *Environmental Research Letters*, **10 (1)**, https://doi.org/10.1088/1748-9326/10/1/014005.

Gervais, M., E. Atallah, J. R. Gyakum, and L. B. Tremblay, 2016: Arctic Air Masses in a Warming World. *Journal of Climate*, **29**, 2359–2373, https://doi.org/10.1175/JCLI-D-15-0499.1.

Gervais, M., J. Shaman, and Y. Kushnir, 2020: Impact of the North Atlantic Warming Hole on Sensible Weather. *Journal of Climate*, **33 (10)**, 4255–4271, https://doi.org/10.1175/jcli-d-19-0636.1.

Grotjahn, R., and Coauthors, 2016: *North American extreme temperature events and related large scale meteorological patterns: a review of statistical methods, dynamics, modeling, and trends*, Vol. 46. Springer Berlin Heidelberg, 1151–1184 pp., https://doi.org/10.1007/s00382-015-2638-6.

Holland, M. M., and C. M. Bitz, 2003: Polar amplification of climate change in coupled models. *Climate Dynamics*, **21 (3-4)**, https://doi.org/10.1007/s00382-003-0332-6.

Hoskins, B. J., M. E. McIntyre, and a. W. Robertson, 1985: On the use and significance of isentropic potential vorticity maps. *Quarterly Journal of the Royal Meteorological Society*, **111 (470)**, 877–946.

Hunke, E. C., W. H. Lipscomb, A. K. Turner, N. Jeffery, and S. Elliot, 2015: CICE: The Los Alamos Sea Ice Model Documentation and Software User's Manual Version 5.1 LA-CC-06-012. *Los Alamos National Laboratory Tech. Rep. LA-CC-06-012*, 76.

Hurrell, J. W., 1995: Decadal trends in the north atlantic oscillation. *Science*, **269**, 676–679.

Hurrell, J. W., and Coauthors, 2013: The community earth system model: A framework for collaborative research. *Bulletin of the American Meteorological Society*, **94**, 1339–1360, https://doi.org/10.1175/BAMS-D-12-00121.1.

Jahn, A., J. E. Kay, M. M. Holland, and D. M. Hall, 2016: How predictable is the timing of a summer ice-free Arctic? *Geophysical Research Letters*, **43 (17)**, 9113–9120, https://doi.org/10.1002/2016GL070067.

Kang, J. M., T. A. Shaw, and L. Sun, 2023: Arctic Sea Ice Loss Weakens Northern Hemisphere Summertime Storminess but Not Until the Late 21st Century. *Geophysical Research Letters*, **50 (9)**, 1–10, https://doi.org/10.1029/2022GL102301.

Kohonen, T., 2001: *Self-Organizing Maps Third Edition*. Springer.

Marsh, D. R., M. J. Mills, D. E. Kinnison, J. F. Lamarque, N. Calvo, and L. M. Polvani, 2013: Climate change from 1850 to 2005 simulated in CESM1(WACCM). *Journal of Climate*, **26 (19)**, 7372–7391, https://doi.org/10.1175/JCLI-D-12-00558.1.

McCusker, K. E., P. J. Kushner, J. C. Fyfe, M. Sigmond, V. V. Kharin, and C. M. Bitz, 2017: Remarkable separability of circulation response to Arctic sea ice loss and greenhouse gas forcing. *Geophysical Research Letters*, **44 (15)**, 7955–7964, https://doi.org/10.1002/2017GL074327.

Oudar, T., E. Sanchez-Gomez, F. Chauvin, J. Cattiaux, L. Terray, and C. Cassou, 2017: Respective roles of direct GHG radiative forcing and induced Arctic sea ice loss on the Northern Hemisphere atmospheric circulation. *Climate Dynamics*, **49**, 3693–3713, https://doi.org/10.1007/s00382-017-3541-0.

Peings, Y., Z. M. Labe, and G. Magnusdottir, 2021: Are 100 Ensemble Members Enough to Capture the Remote Atmospheric Response to +2°C Arctic Sea Ice Loss? *Journal of Climate*, **34 (10)**, 3751–3769, https://doi.org/10.1175/jcli-d-20-0613.1.

Perlwitz, J., M. Hoerling, and R. Dole, 2015: Arctic Tropospheric Warming: Causes and Linkages to Lower Latitudes. *Journal of Climate*, **28 (6)**, 2154–2167, https://doi.org/10.1175/JCLI-D-14-00095.1.

Pithan, F., and T. Mauritsen, 2014: Arctic amplification dominated by temperature feedbacks in contemporary climate models. *Nature Geoscience*, **7**, 181–184, https://doi.org/10.1038/NGEO2071.

Ronalds, B., E. A. Barnes, R. Eade, Y. Peings, and M. Sigmond, 2020: North Pacific zonal wind response to sea ice loss in the Polar Amplification Model Intercomparison Project and its downstream implications. *Climate Dynamics*, **55 (7-8)**, 1779–1792, https://doi.org/10.1007/s00382-020-05352-w, URL https://doi.org/10.1007/s00382-020-05352-w.

Screen, J., 2014: Arctic amplification decreases temperature variance in northern mid- to high-latitudes. *Nature Climate Change*, **4**, 577–582, https://doi.org/10.1038/NCLIMATE2268.

Screen, J., C. Deser, and I. Simmonds, 2012: Local and remote controls on observed Arctic warming. *Geophysical Research Letters*, **39**, 1–5, https://doi.org/10.1029/2012GL051598.

Screen, J., and I. Simmonds, 2010: The central role of diminishing sea ice in recent Arctic temperature amplification. *Nature*, **464**, 1334–1337, https://doi.org/10.1038/nature09051, URL http://dx.doi.org/10.1038/nature09051.

Screen, J., I. Simmonds, C. Deser, and R. Tomas, 2013: The Atmospheric Response to Three Decades of Observed Arctic Sea Ice Loss. *Journal of Climate*, **26 (4)**, 1230–1248, https://doi.org/10.1175/JCLI-D-12-00063.1, URL http://journals.ametsoc.org/doi/abs/10.1175/JCLI-D-12-00063.1.

Screen, J. A., C. Deser, and L. Sun, 2015: Reduced Risk of North American Cold Extremes due to Continued Arctic Sea Ice Loss. *Bulletin of the American Meteorological Society*, **96 (9)**, 1489–1503, https://doi.org/10.1175/BAMS-D-14-00185.1.

Screen, J. A., and Coauthors, 2018: Consistency and discrepancy in the atmospheric response to Arctic sea-ice loss across climate models. *Nature Geoscience*, **11 (3)**, 155–163, https://doi.org/10.1038/s41561-018-0059-y, URL http://dx.doi.org/10.1038/s41561-018-0059-y.

Serreze, M. C., a. P. Barrett, J. C. Stroeve, D. N. Kindig, and M. M. Holland, 2009: The emergence of surface-based Arctic amplification. *The Cryosphere Discussions*, **2**, 601–622, https://doi.org/10.5194/tcd-2-601-2008.

Singarayer, J., J. Bambier, and P. Valdes, 2006: Twenty-First-Century Climate Impacts from a Declining Arctic Sea Ice Cover. *Journal of Climate*, **19**, 1109–1125, URL https://doi.org/10.1175/JCLI3649.1.

Smith, D., and Coauthors, 2019: The Polar Amplification Model Intercomparison Project (PAMIP) contribution to CMIP6: investigating the causes and consequences of polar amplification. *Geoscientific Model Development*, **12**, 1–42, https://doi.org/10.5194/gmd-2018-82.

Smith, D. M., N. J. Dunstone, A. A. Scaife, E. K. Fiedler, D. Copsey, and S. C. Hardiman, 2017: Atmospheric response to Arctic and Antarctic sea ice: The importance of ocean-atmosphere coupling and the background state. *Journal of Climate*, **30 (12)**, 4547–4565, https://doi.org/10.1175/JCLI-D-16-0564.1.

Sun, L., C. Deser, and R. A. Tomas, 2015: Mechanisms of stratospheric and tropospheric circulation response to projected Arctic sea ice loss. *Journal of Climate*, **28 (19)**, 7824–7845, https://doi.org/10.1175/JCLI-D-15-0169.1.

Thompson, D. W. J., and J. M. Wallace, 1998: The Arctic oscillation signature in the wintertime geopotential height and temperature fields. *Geophysical Research Letters*, **25 (9)**, 1297, https://doi.org/10.1029/98GL00950.

Vesanto, J., J. Himberg, E. Alhoniemi, and J. Parhankangas, 2000: SOM Toolbox for Matlab 5. Tech. Rep. 0, Helsinki Univiversity of Technology, Helsinki, Finland.

Vihma, T., 2014: Effects of Arctic Sea Ice Decline on Weather and Climate : A Review. *Surveys in Geophysics*, **35**, 1175–1214, https://doi.org/10.1007/s10712-014-9284-0.

Wallace, J., and D. Gutzler, 1981: Teleconnections in the Geopotential Height Field during the Northern Hemisphere Winter. *Monthly Weather Review*, **109**, 784–812, URL https://doi.org/10.1175/1520-0493(1981)109%3C0784:TITGHF%3E2.0.CO;2.

Walsh, J. E., a. S. Phillips, D. H. Portis, and W. L. Chapman, 2001: Extreme cold outbreaks in the United States and Europe, 1948-99. *Journal of Climate*, **14 (1987)**, 2642–2658, https://doi.org/10.1175/1520-0442(2001)014⟨2642:ECOITU⟩2.0.CO;2.

Wang, M., and J. E. Overland, 2012: A sea ice free summer Arctic within 30 years: An update from CMIP5 models. *Geophysical Research Letters*, **39 (18)**, n/a–n/a, https://doi.org/10.1029/2012GL052868, URL http://doi.wiley.com/10.1029/2012GL052868.